γ-Agostic Interactions in (MesCCC)Fe-Mes(L) Complexes

Daniel C. Najera,[a] Marconi N. Peñas de Frutos,[b,c] Max García-Melchor,[b]* Alison R. Fout[a]*

[a] School of Chemical Sciences, University of Illinois at Urbana-Champaign, 600 S. Mathews Ave., Urbana, Illinois 61801, USA.

[b] School of Chemistry, CRANN and AMBER Research Centres, Trinity College Dublin, College Green, Dublin 2, Ireland.

[c] Universidad de Valladolid, Valladolid, Spain.

Supporting Information Table of Contents:

General Considerations. All manipulations of air- and moisture-sensitive compounds were carried out in the absence of water and dioxygen in an MBraun inert atmosphere glovebox under a dinitrogen atmosphere except where specified otherwise. All glassware was oven dried for a minimum of 8 h and cooled in an evacuated antechamber prior to use in the glovebox. Solvents for sensitive manipulations were dried and deoxygenated on a Glass Contour System (SG Water USA, Nashua, NH) and stored over 4 Å molecular sieves purchased from Strem following a literature procedure prior to use.[1] The ligand precursor salt $[H_3(^{Mes}CCC)]Cl_2$,[2] and Fe_2Mes_4[3] were prepared according to literature procedures. Benzene-d_6 and toluene-d_8 were purchased from Cambridge Isotope Labs and were degassed and stored over 4 Å molecular sieves prior to use. Lithium hexamethyldisilazide ($LiN(SiMe_3)_2$), PPh_3, and BPh_3 were purchased from MilliporeSigma and recrystallized from toluene or hexanes prior to use. Trimethylphosphine (PMe_3, 1.0 M in THF) was purchased from MilliporeSigma. Pyridine and 3,5-lutidine were purchased from MilliporeSigma, degassed and stored over 4 Å molecular sieves prior to use. Celite® 545 (J. T. Baker) was dried in a Schlenk flask for 24 h under dynamic vacuum while heating to at least 150˚C prior to use in a glovebox.

NMR Spectra were recorded at room temperature on a Bruker spectrometer operating at 600 MHz (^1H), 151 MHz (^{13}C), and 243 MHz (^{31}P) and referenced to the residual HC_6D_5 and HC_7D_7 resonance (δ in parts per million, and J in Hz). Solid-state infrared spectra were recorded using a PerkinElmer Frontier FT-IR spectrophotometer equipped with a KRS5 thallium bromide/iodide Universal Attenuated Total Reflectance accessory. Elemental analyses were performed by the University of Illinois at Urbana-Champaign School of Chemical Sciences Microanalysis Laboratory in Urbana, IL. Mass Spectrometry analyses were performed by the University of Illinois at Urbana-Champaign Mass Spectrometry Laboratory. X-ray crystallography was performed at the George L. Clark X-ray Facility at UIUC. Single-crystal X-ray diffraction data were collected with the use of multimirror monochromatized Mo Kα radiation (0.71073 Å) at 100 K on a Bruker D8 Venture diffractometer equipped with a Photon 100 detector. Combinations of 0.5° φ and ω scans were used to collect the data. The collection, cell refinement, and integration of intensity data were carried out with the APEX2 software.[4] Multi-scan absorption correction was performed using SADABS.[5] The structures were solved with XT[6] and refined with the full-matrix least-squares SHELXL[7] program within the Olex2[8] refinement GUI. All structureswere submitted to the Cambridge Structural Database with structure numbers 2177566-2177571.

Synthesis of Metal Complexes

Synthesis of (^Mes^CCC)FeMes(Py) (1-Py). A 20 mL scintillation vial equipped with a stir bar was charged with [H$_3$(^Mes^CCC)]Cl$_2$ (0.100 g, 0.161 mmol, 1.0 equiv.) and toluene (2 mL). To the suspension, a solution of LiN(SiMe$_3$)$_2$ (0.057 g, 0.323 mmol, 2.1 equiv.) in toluene (2 mL) was added dropwise and the mixture was stirred at room temperature for 5 min. Afterwards, a cold (-35 °C) solution of Fe$_2$Mes$_4$ (0.047 g, 0.080 mmol, 0.5 equiv.) and 5 drops of pyridine in toluene (2 mL) was added dropwise resulting in a gradual color change to dark purple. After stirring at room temperature for 4 h, the suspension was filtered over Celite. Volatiles were removed under reduced pressure and the solid residue was washed with HMDSO (3 x 3 mL) and extracted in diethyl ether. The solvent was evaporated under reduced pressure. The product was then lyophilized from benzene to give a dark purple powder in good yield (0.121 g, 0.151 mmol, 94%). Crystals suitable for X-ray diffraction were grown from a concentrated toluene solution of the product at -35 °C. Anal. Calcd. for C$_{52}$H$_{49}$FeN$_5$: C, 78.09; H, 6.17; N, 8.76. Found C, 77.83; H, 6.24; N, 8.67. NMR data (C$_6$D$_6$, 25 °C): ^{1}H δ = 8,04 (d, J = 7.9, 2H), 7.77 (d, J = 7.4 2H), 7.57 (d, J = 6.9 Hz, 2H), 7.50 (t, J = 7.7, 1H), 7.10 (t, J = 7.6, 2H), 6.95 (t, J = 7.7, 2H), 6.78 (d, J = 8.0, 4H), 6.63(d, J = 7.8, 2H), 6.25-6.23 (m, 2H), 5.83 (s, 1H), 5.77 (t, J = 2H), 2.29 (s, 3H), 2.14 (s, 6H), 1.45 (s, 6H), 1.16 (s, 6H), 0.92 (s, 3H), -0.55 (s, 3H). ^{13}C{^{1}H} δ = 224.71, 199.79, 162.09, 152.72, 145.67, 140.83, 138.68, 138.38, 136.70, 135.02, 133.21, 132.41, 131.23, 129.72, 129.33, 126.08, 125.70, 124.38, 122.85, 121.90, 121.63, 117.88, 109.64, 108.68, 105.08, 23.79, 21.44, 21.17, 21.04, 17.32, 16.50, 5.60.

Synthesis of (^Mes^CCC)FeMes(3,5-Lu) (1-Lu). A 20 mL scintillation vial equipped with a stir bar was charged with [H$_3$(^Mes^CCC)]Cl$_2$ (0.100 g, 0.161 mmol, 1.0 equiv.) and toluene (2 mL). To the suspension, a solution of LiN(SiMe$_3$)$_2$ (0.057 g, 0.323 mmol, 2.1 equiv.) in toluene (2 mL) was added dropwise and the mixture was stirred at room temperature for 5 min. Afterwards, a cold (-35 °C) solution of Fe$_2$Mes$_4$ (0.047 g, 0.080 mmol, 0.5 equiv.) and 5 drops of 3,-5-Lutidine in toluene (2 mL) was added dropwise resulting in a gradual color change to dark purple. After stirring at room temperature for 4 h, the suspension was filtered over Celite. Volatiles were removed under reduced pressure and the solid residue was washed with HMDSO (3 x 3 mL) and extracted in diethyl ether. The solvent was evaporated under reduced pressure. The product was then lyophilized from benzene to give a dark purple powder in good yield (0.123 g, 0.149 mmol, 93%). Crystals suitable for X-ray diffraction were grown from slow evaporation of a concentrated solution of the product in a 1:1 mixture of diethyl ether and HMDSO. Anal. Calcd. for C$_{54}$H$_{53}$FeN$_5$: C, 78.34; H, 6.47; N, 8.46. Found C, 77.05; H, 6.36; N, 8.30. NMR data (C$_6$D$_6$, 25 °C): ^{1}H NMR δ = 8.02 (d, J = 8.06 Hz, 2H), 7.78 (d, J = 7.7 Hz, 2H), 7.53 (t, J = 7.6, 1H), 7.33 (s, 2H), 7.07 (t, J = 7.6 Hz, 2H), 6.93 (t, J = 7.6 Hz, 2H), 6.79 (s, 4H), 6.63 (d, J = 7.8 Hz 2H), 6.23 (s, 1H), 6.04 (s, 1H), 5.85 (s, 1H), 2.29 (s, 3H), 2.12 (s, 6H), 1.53 (s, 6H), 1.36 (s, 6H), 1.19 (s, 6H), 0.92 (s, 3H), -0.45 (s, 3H). ^{13}C{^{1}H} δ = δ 224.80, 200.28, 162.21, 152.81, 150.06, 145.74, 140.89, 138.68, 138.44, 136.84, 135.14, 133.58, 133.26, 132.52, 131.80, 129.75, 128.68, 128.59, 126.11, 124.34, 121.83, 121.55, 117.67, 109.62, 108.57, 105.02, 23.83, 21.18, 21.03, 17.68, 16.90, 16.57, 6.05.

Synthesis of (^Mes^CCC)FeMes(PPh$_3$) (1-PPh$_3$). A 20 mL scintillation vial equipped with a stir bar was charged with [H$_3$(^Mes^CCC)]Cl$_2$ (0.100 g, 0.161 mmol, 1.0 equiv.) and toluene (2 mL). To the suspension, a solution of LiN(SiMe$_3$)$_2$ (0.057 g, 0.323 mmol, 2.1 equiv.) in toluene (2 mL) was added dropwise and the mixture was stirred at room temperature for 5 min. Afterwards, triphenylphosphine was added in 1 mL of toluene, followed by a cold (-35 °C) solution of Fe$_2$Mes$_4$ (0.047 g, 0.080 mmol, 0.5 equiv.) in toluene (2 mL), resulting in a gradual color change to orange. After stirring at room temperature for 4 h, the suspension was filtered over Celite. Volatiles were removed under reduced pressure and the solid residue was washed with hexanes (3 x 3 mL) and lyophilized from benzene to give a bright orange powder

in good yield (0.134 g, 0.136 mmol, 85%). Crystals suitable for X-ray diffraction were grown from a concentrated diethyl ether solution of the product with 1 drop of HMDSO. Anal. Calcd. for $C_{65}H_{59}FeN_4P$: C, 79.42; H, 6.05; N, 5.70. Found C, 79.79; H, 6.32; N, 5.52. NMR data (C_6D_6, 25 °C): ^1H δ = 7.81 (d, J = 8.1, 2H), 7.39 (t, J = 7.9 2H), 7.33(d, J = 7.5 Hz, 2H), 7.23 (t, J = 7.6, 1H), 7.10 (t, J = 7.8 Hz, 2H), 7.04 (t, J = 7.5, 3H), 6.92 (t, J = 7.5, 2H), 6.74–6.68(m, 8H), 6.59–6.51 (m, 8H) 6.13 (s, 1H), 5.32 (s, 1H), 2.18 (s, 3H), 2.09 (s, 6H), 1.71 (s, 6H) 0.95 (s, 3H), 0.89 (s, 6H), -1.84 (d, J = 1.4 Hz, 3H). $^{13}C\{^1H\}$ δ = 226.22 (d, J = 10.3 Hz), 187.30 (d, J = 15.2 Hz), 157.28 (d, J = 16.7 Hz), 150.36, 145.63, 141.33, 139.59, 138.34, 137.56 (t, J = 8.2 Hz), 137.49, 137.07, 136.99, 136.84, 135.11 (d, J = 12.2 Hz), 134.54, 133.25, 132.78 (d, J = 8.9 Hz), 129.59, 129.38, 127.08 (d, J = 7.6 Hz), 125.58 (d, J = 3.8 Hz), 125.56, 121.64 (d, J = 24.4 Hz), 118.36, 109.75, 108.72, 105.40, 21.99, 21.05, 20.88, 18.67, 16.38, 0.83. $^{31}P\{^1H\}$ δ = 42.29.

Synthesis of (^{Mes}CCC)FeMes(NCMe) (1-NCMe). A 20 mL scintillation vial equipped with a stir bar was charged with **1-Py** (0.050 g, 0.063 mmol, 1.0 equiv.) and dissolved in Et_2O (1 mL). To this vial, acetonitrile (2 mL) was added, resulted in an immediate color change to burgundy. After stirring at room temperature for 20 min, the suspension was filtered over Celite. The resulting solution was concentrated to *ca.* 1 mL and placed in the freezer (-35 °C) overnight to crystallize. The crystals were isolated by decanting the mother liquor giving the product (0.017 g, 0.022 mmol, 35%). Crystals suitable for X-ray diffraction were grown from a concentrated solution of the product in acetonitrile-d_3. NMR data (C_6D_6, 25 °C): ^1H δ = δ 8.01 (d, J = 8.1 Hz, 2H), 7.70 (d, J = 7.6 Hz, 2H), 7.46 (t, J = 7.6 Hz, 1H), 7.10 (t, J = 7.6 Hz, 2H), 6.99 (t, J = 7.6 Hz, 2H), 6.83 – 6.71 (m, 6H), 6.20 (s, 1H), 5.60 (s, 1H), 2.25 (s, 3H), 2.21 (s, 6H), 2.11 (s, 6H), 1.16 (s, 6H), 0.97 (s, 3H), 0.36 (s, 3H), -1.26 (s, 3H). $^{13}C\{^1H\}$ δ = 224.83, 194.73, 161.15, 151.91, 144.91, 140.46, 138.61, 138.26, 136.44, 135.04, 133.53, 133.22, 131.56, 129.64, 125.78, 124.70, 121.77, 117.89, 109.69, 108.69, 105.14, 23.22, 21.15, 21.10, 17.91, 16.38, 2.92, 1.45, 0.09. ATR-IR = 2224 cm^{-1} (C≡N). Decomposition of the product at room temperature precluded characterization by CHN analysis.

Synthesis of (^{Mes}CCC)FeMes(PMe₃) (1-PMe₃). A 20 mL scintillation vial equipped with a stir bar was charged with **1-Py** (0.050 g, 0.063 mmol, 1.0 equiv.) and THF (4 mL). To this solution, PMe_3 (1.0 M, 0.069 mL, 0.069 mmol, 1.1 equiv) was added dropwise via syringe. After stirring at room temperature for 20 min, the solution was filtered over Celite and volatiles were removed under reduced pressure. The residue was washed with HMDSO (2 x 2 mL) and extracted in THF. Removal of the solvent under reduced pressure gives the product as an orange powder (0.044 g, 0.055 mmol, 87%). Crystals suitable for X-ray diffraction were grown from HMDSO at -37 °C. Anal. Calcd. for $C_{50}H_{53}FeN_4P$: C, 75.37; H, 6.70; N, 7.03. Found C, 75.48; H, 6.92; N, 7.02. NMR data (C_6D_6, 25 °C): ^1H δ = 7.99 (d, J = 8.0 Hz, 2H), 7.64 (d, J = 7.7 Hz, 2H), 7.39 (t, J = 7.6 Hz, 1H), 7.12 (t, J = 7.6 Hz, 2H), 6.98 (t, J = 7.6 Hz, 2H), 6.72 (s, 2H), 6.65 (d, J = 7.8 Hz, 2H), 6.63 (s, 2H), 6.24 (s, 1H), 5.39 (s, 1H), 2.25 (s, 3H), 2.20 (s, 6H), 2.09 (s, 6H), 1.05 (s, 3H), 1.02 (s, 6H), 0.43 (d, J = 6.3 Hz , 9H), -2.25 (s, 3H).$^{13}C\{^1H\}$ δ = 226.69 (d, J = 13.2 Hz), 187.79, 162.79, 149.23, 145.45, 141.35, 138.95, 138.30, 136.49, 135.69, 134.41, 132.72, 129.90, 129.31, 126.24, 125.67, 125.64, 121.96, 121.74, 117.58, 109.73, 108.64, 105.00, 34.98, 25.64, 21.11, 21.04, 19.46, 16.19, 15.39 (d, J = 19.2 Hz), -2.05. ^{31}P δ = 10.64.

Synthesis of [^{Mes}CCC)FeMes]₂(μ-N₂) (1-N₂). A 20 mL scintillation vial equipped with a stir bar was charged with **1-Py** (0.050 g, 0.063 mmol, 2.0 equiv.) and pentane (5 mL). To this vial was added a suspension of BPh_3 (0.015 g, 0.063 mmol, 2.0 equiv) in pentane (2 mL), resulting in a gradual color change from purple to dark green. After stirring at room temperature for 2 h, the suspension was filtered over Celite and volatiles were removed under reduced pressure. The solid residue was extracted in cold (-35

°C) pentane (4 x 1 mL) and filtered over Celite. The solvent was removed under reduced pressure to give a dark green powder (0.035 g, 0.024 mmol, 76%). Crystals suitable for X-ray diffraction were grown from a concentrated of the product in hexanes at -35 °C. NMR data (C_6D_6, 25 °C): ^1H δ = 8.07 (d, J = 8.0 Hz, 2H), 7.62 (d, J = 7.9 Hz, 2H), 7.39 – 7.35 (m, 3H), 7.25 (s, 2H), 7.09 (t, J = 7.6 Hz, 2H), 7.02 (t, J = 7.7 Hz, 2H), 6.95 (d, J = 7.5 Hz, 4H), 6.68 (dt, J = 20.9, 7.8 Hz, 7H), 6.60 (d, J = 7.9 Hz, 2H), 6.42 (d, J = 13.4 Hz, 4H), 6.03 (s, 2H), 5.32 (s, 2H), 2.53 (s, 6H), 2.13 (s, 6H), 2.10 (s, 6H) 1.83 (s, 6H), 1.67 (s, 6H), 0.97 (s, 6H), 0.86 (s, 6H), 0.78 (s, 6H), -1.84 (s, 6H). Thermal instability of the product precluded characterization by ^{13}C NMR spectroscopy and CHN analysis.

Synthesis of (^{Mes}CCC)FeMes(CO) (1-CO). A 20 mL Schlenk tube was charged with **1-Py** (0.050 g, 0.063 mmol, 1.0 equiv.) and THF (4 mL). This solution was taken out of the glovebox and subjected to 3 freeze-pump-thaw cycles followed by addition of CO (1 atm, 25 °C. The flask was brought back into the glovebox, shaken for 10 seconds until the solution turned orange. The solution was filtered over Celite and volatiles removed under reduced pressure. The residue was washed with pentane (3 x 3 mL) and extracted in THF. Removal of the solvent under reduced pressure furnished the product as a light orange powder (0.034 g, 0.045 mmol, 71%). NMR data (C_6D_6, 25 °C): ^1H δ = 7.79 (d, J = 8.0 Hz, 2H), 7.50 (d, J = 7.8 Hz, 2H), 7.34 (t, J = 7.8 Hz, 1H), 7.06 (t, J = 7.7 Hz, 2H), 6.91 (t, J = 7.6 Hz, 2H), 6.60 (d, J = 8.3 Hz, 4H), 6.57 (s, 2H), 6.37 (s, 1H), 5.59 (d, J = 1.7 Hz, 1H), 2.36 (s, 6H), 2.18 (s, 3H), 2.01 (s, 7H), 1.33 (s, 3H), 1.04 (s, 6H), -2.33 (s, 3H). $^{13}C\{^1H\}$ δ = 217.52, 206.76, 169.90, 157.00, 147.90, 144.79, 139.13, 138.82, 137.76, 137.37, 137.03, 133.56, 132.21, 130.70, 129.22, 129.17, 127.47, 126.29, 122.78, 122.49, 121.32, 110.92, 109.74, 107.39, 22.15, 21.02, 20.98, 18.15, 16.28, -4.92. ATR-IR = 1910 cm^{-1} (C≡O). A persistent impurity of THF and **2** precluded CHN analysis. HRMS (ESI) calcd. for [M – CO]$^+$: 720.2915; found: 720.2903

Synthesis of (^{Mes}CCC)Fe(COMes)(CO)$_2$ (2). A 20 mL Schlenk tube equipped with a stir bar was charged with **1-Py** (0.050 g, 0.063 mmol, 1.0 equiv.) and THF (4 mL). This solution was taken out of the glovebox and subjected to 3 freeze-pump-thaw cycles followed by addition of CO (1 atm, 25 °C), resulting in an immediate color change from purple to orange. The flask was brought back into the glovebox and stirred until the solution turned yellow (*ca.* 2 h). The solution was filtered over Celite and volatiles removed under reduced pressure. The residue was washed with HMDSO (2 x 2 mL) and pentane (2 x 2 mL) and extracted in THF. Removal of the solvent under reduced pressure afforded the product as a tan solid (0.047 g, 0.058 mmol, 92%). Anal. calcd. for $C_{50}H_{44}FeN_5O_3$: C, 74.62; H, 5.51; N, 6.96. Found C, 73.12; H, 5.72; N, 6.99. NMR data (C_6D_6, 25 °C): ^1H δ = 7.80 (d, J = 8.1 Hz, 1H), 7.55 (d, J = 7.8 Hz, 1H), 6.90 (t, J = 7.6 Hz, 1H), 6.83 (s, 1H), 6.65 (s, 1H), 6.59 (d, J = 8.0 Hz, 1H), 6.24 (s, 1H), 2.04 (s, 2H), 2.00 (d, J = 7.4 Hz, 4H), 1.84 (s, 2H), 1.58 (s, 3H). $^{13}C\{^1H\}$ δ =. 215.45, 211.99, 211.25, 175.48, 153.42, 147.41, 139.23, 138.19, 138.06, 136.58, 133.78, 133.69, 132.26, 129.88, 129.86, 129.41, 123.83, 123.37, 122.98, 111.18, 110.82, 109.19, 21.04, 20.70, 18.95, 18.53, 18.01. ATR-IR. 1988 (C≡O), 1934 (C≡O), 1589 (C=O). HRMS (ESI) calcd. for $C_{50}H_{45}FeN_4O_3$ [M + H]$^+$: 805.2835; found: 805.2849.

NMR spectra of Metal Complexes

NMR spectra of (^{Mes}CCC)FeMes(Py)
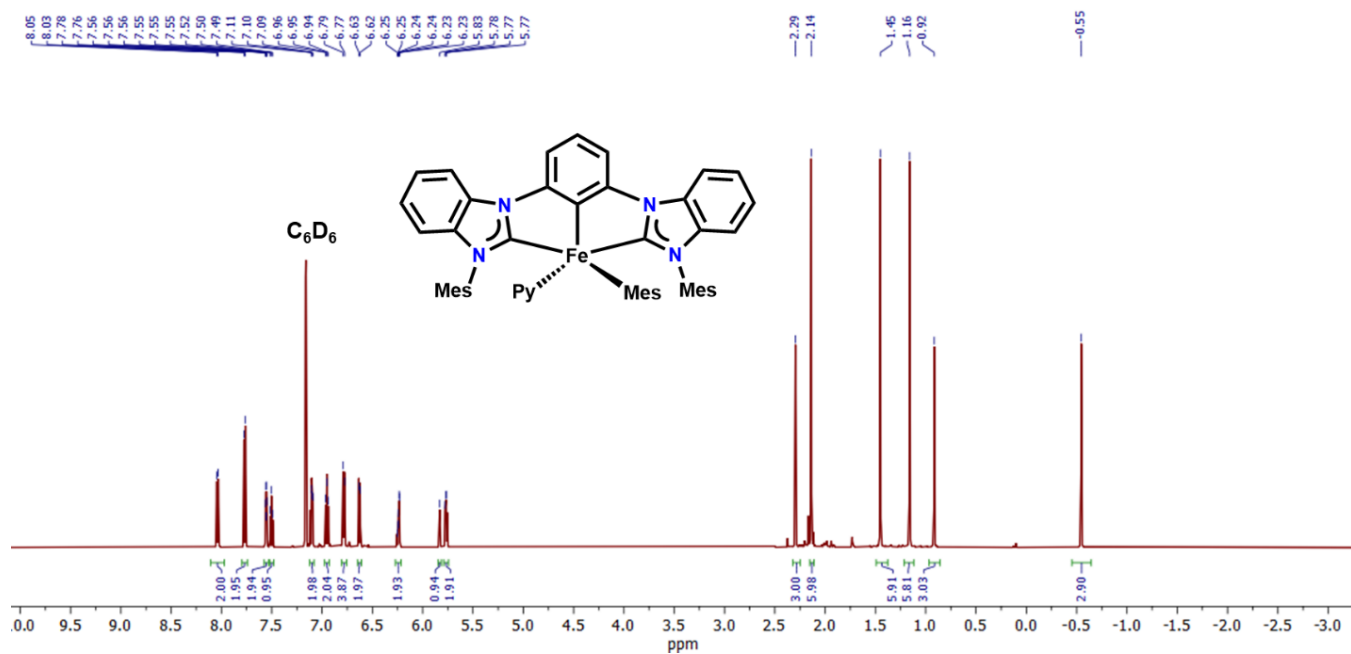
Figure S1. ^{1}H NMR spectrum of (^{Mes}CCC)FeMes(Py) in C$_6$D$_6$.
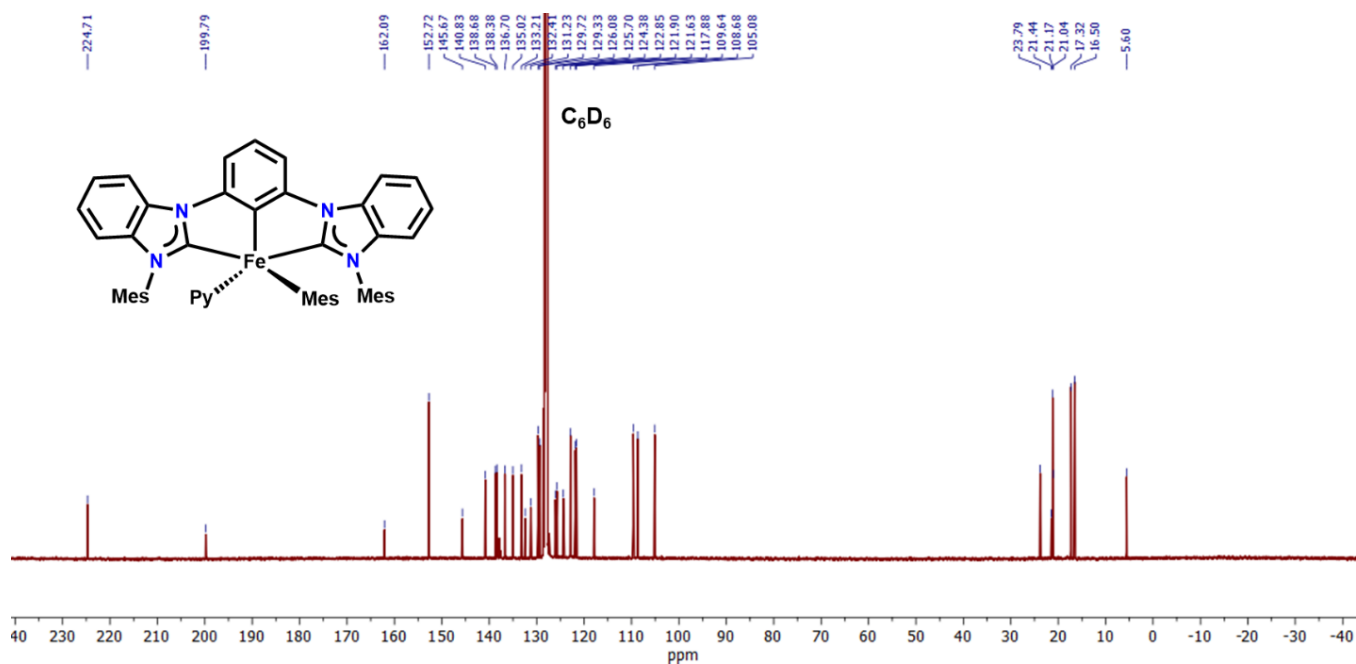
Figure S2. ^{13}C{^{1}H} NMR spectrum of **1-Py** in C$_6$D$_6$.

NMR spectra of (^{Mes}CCC)FeMes(3,5-Lu)
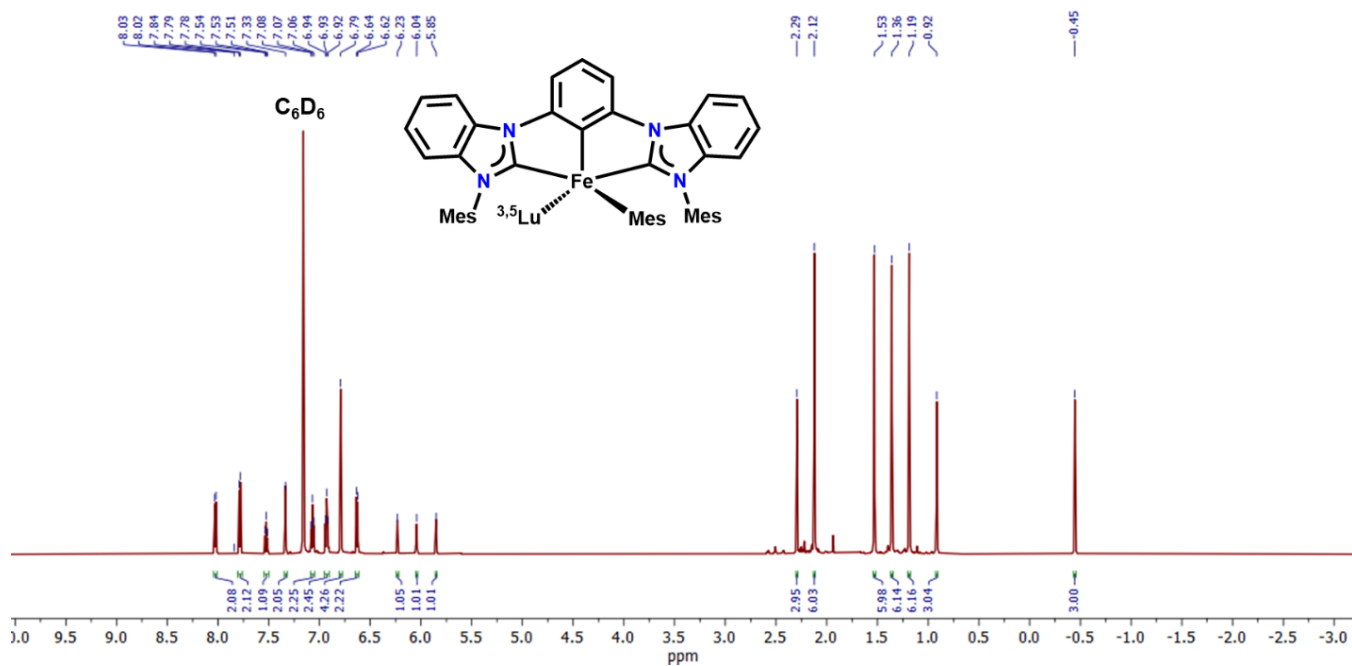
Figure S3. ^{1}H NMR spectrum of **1-Lu** in C$_6$D$_6$.
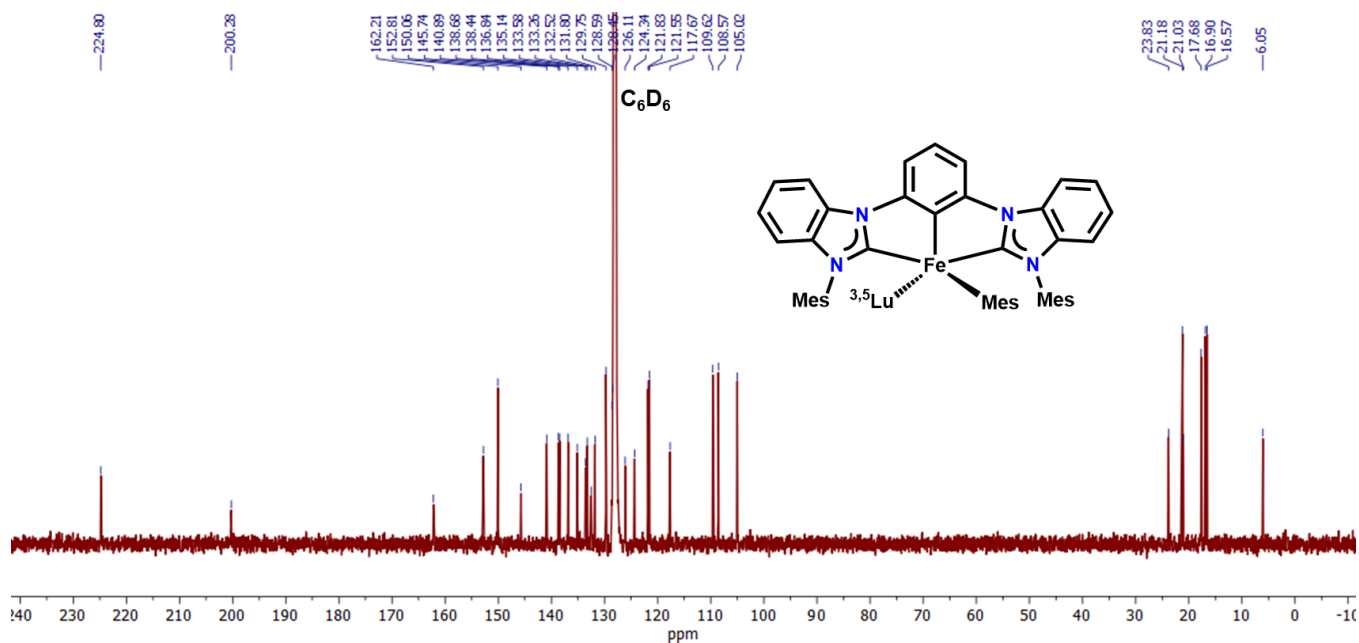
Figure S4. ^{13}C{^{1}H} NMR spectrum of **1-Lu** in C$_6$D$_6$.

NMR spectra of (^{Mes}CCC)FeMes(PPh₃)
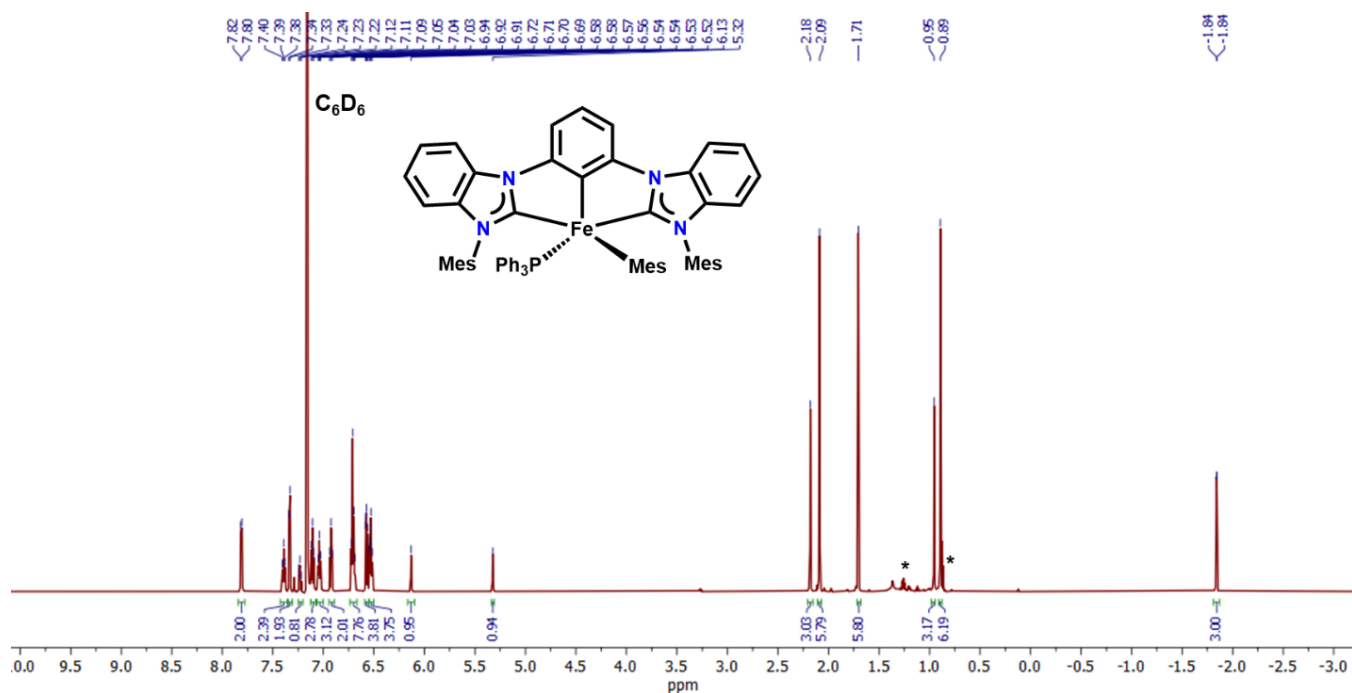
Figure S5. ¹H NMR spectrum of **1-PPh₃** in C₆D₆ (*denotes pentane).
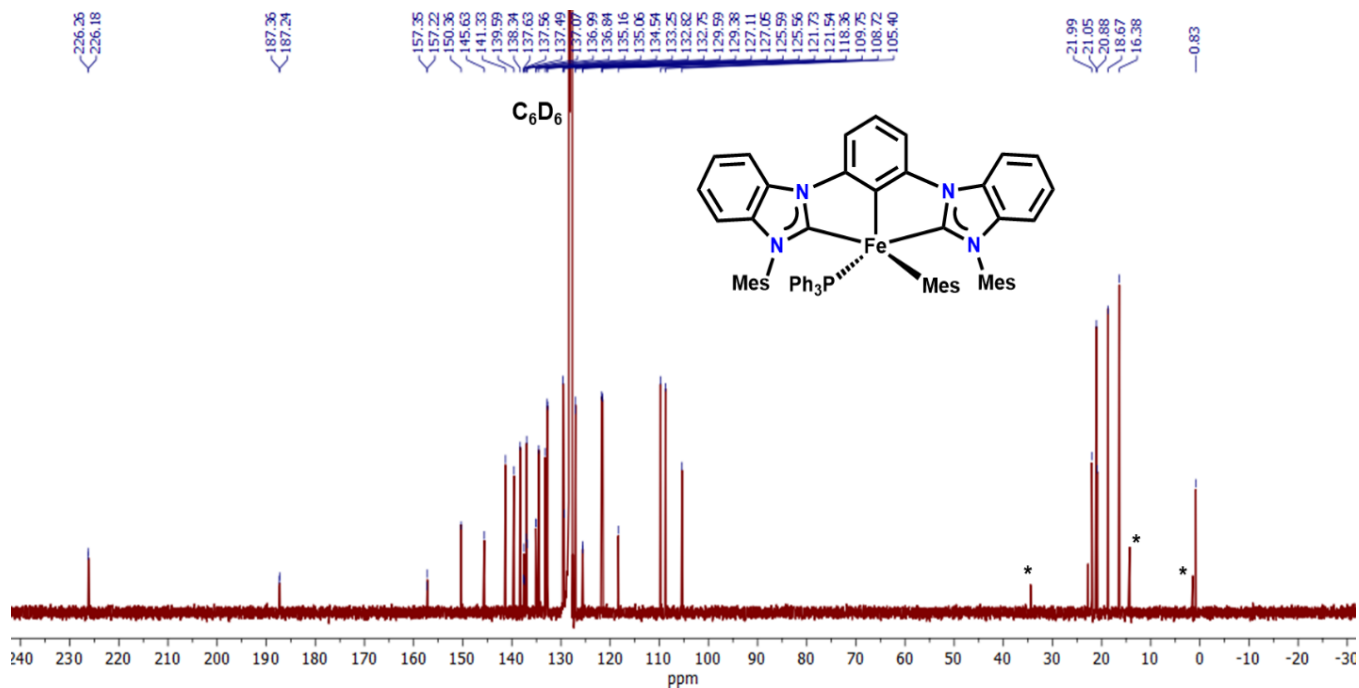
Figure S6. ¹³C{¹H} NMR spectrum of **1-PPh₃** in C₆D₆ (*denotes pentane).
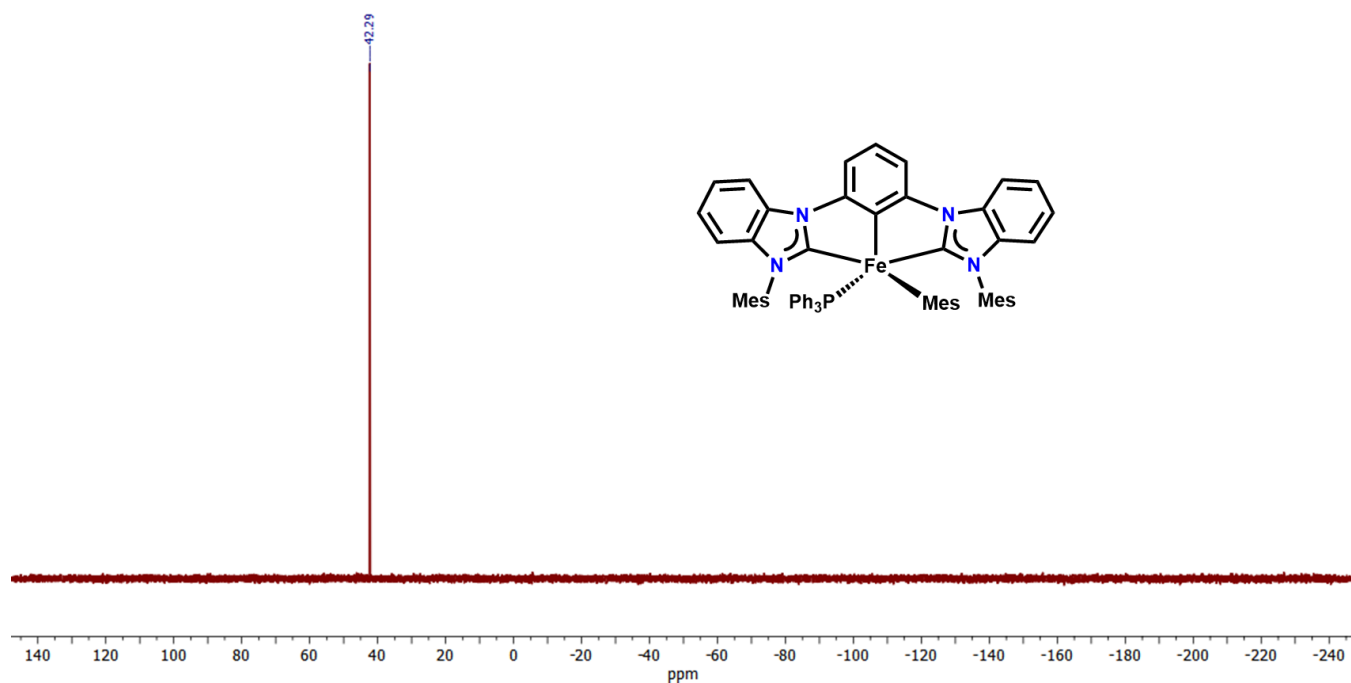
Figure S7. $^{31}P\{^1H\}$ NMR spectrum of **1-PPh₃** in C₆D₆.

NMR spectra of (^{Mes}CCC)FeMes(NCMe)
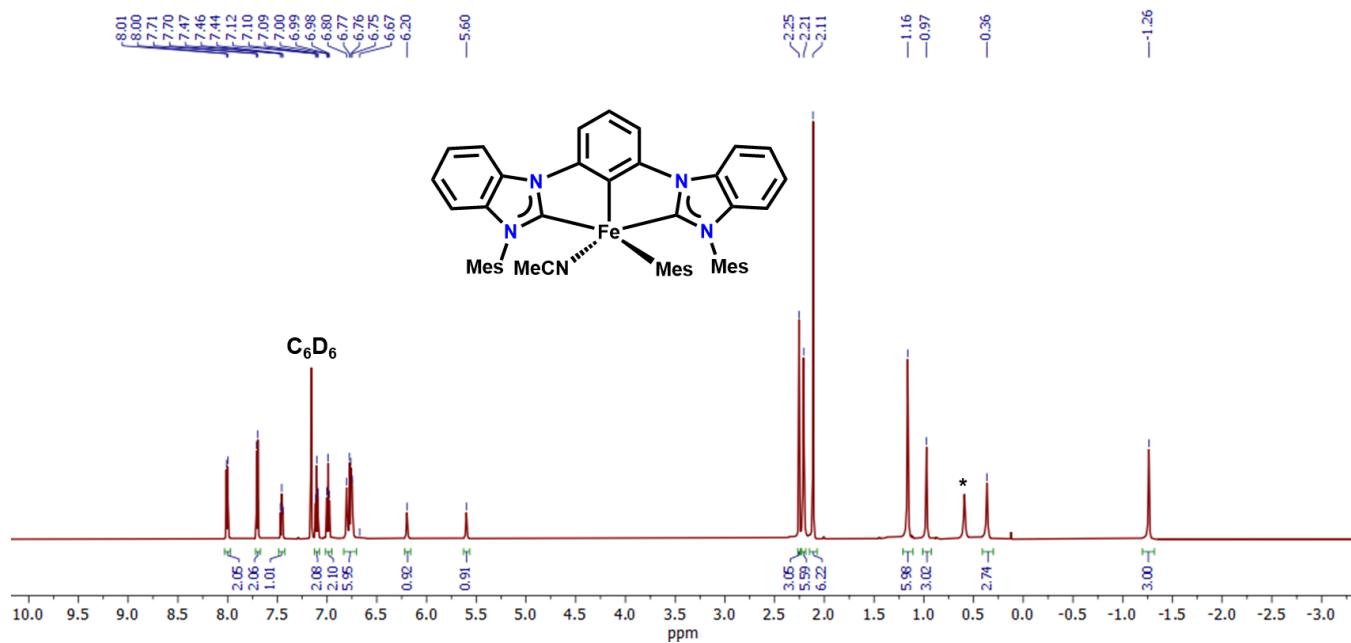
Figure S8. ^1H NMR spectrum of **1-NCMe** in C₆D₆ (*denotes acetonitrile).
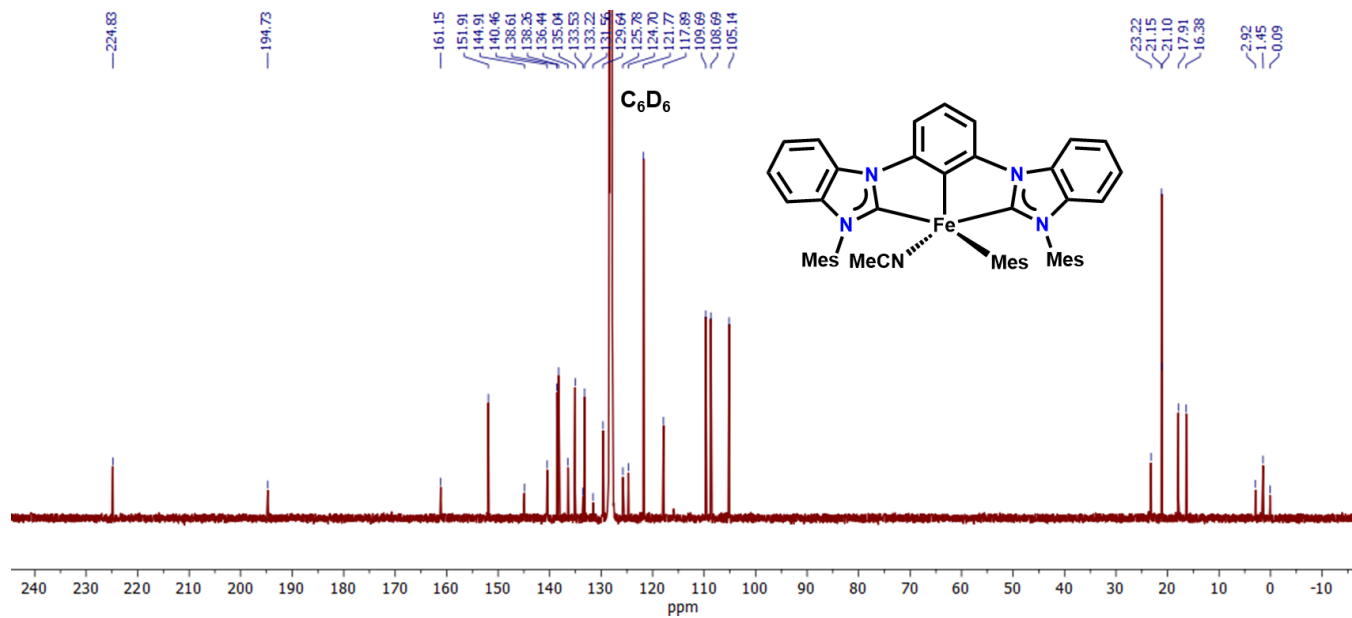
Figure S9. $^{13}C\{^1H\}$ NMR spectrum of **1-NCMe** in C_6D_6.

NMR spectra of (^{Mes}CCC)FeMes(PMe$_3$)
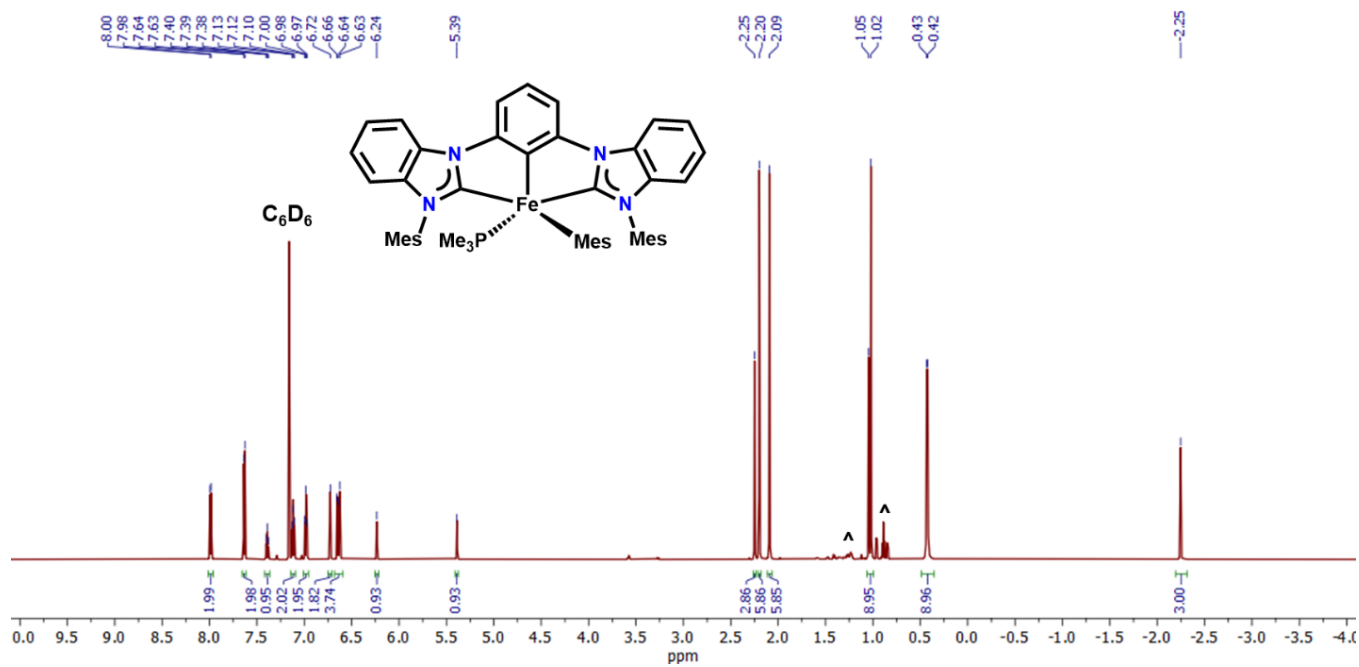
Figure S10. ^1H NMR spectrum of **1-PMe$_3$** in C_6D_6. (^ denotes hexanes).
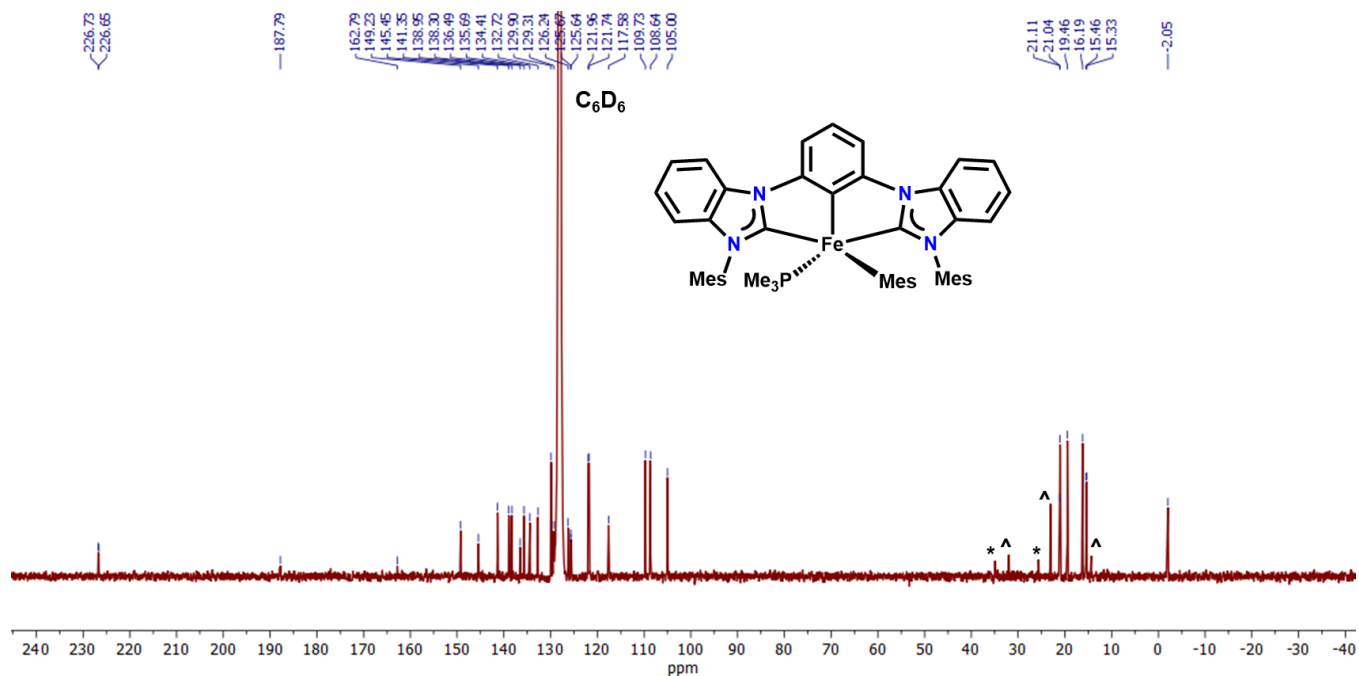
Figure S11. ^{13}C{^{1}H} NMR spectrum of **1-PMe₃** in C₆D₆. (^ denotes hexane, * denotes pentane).
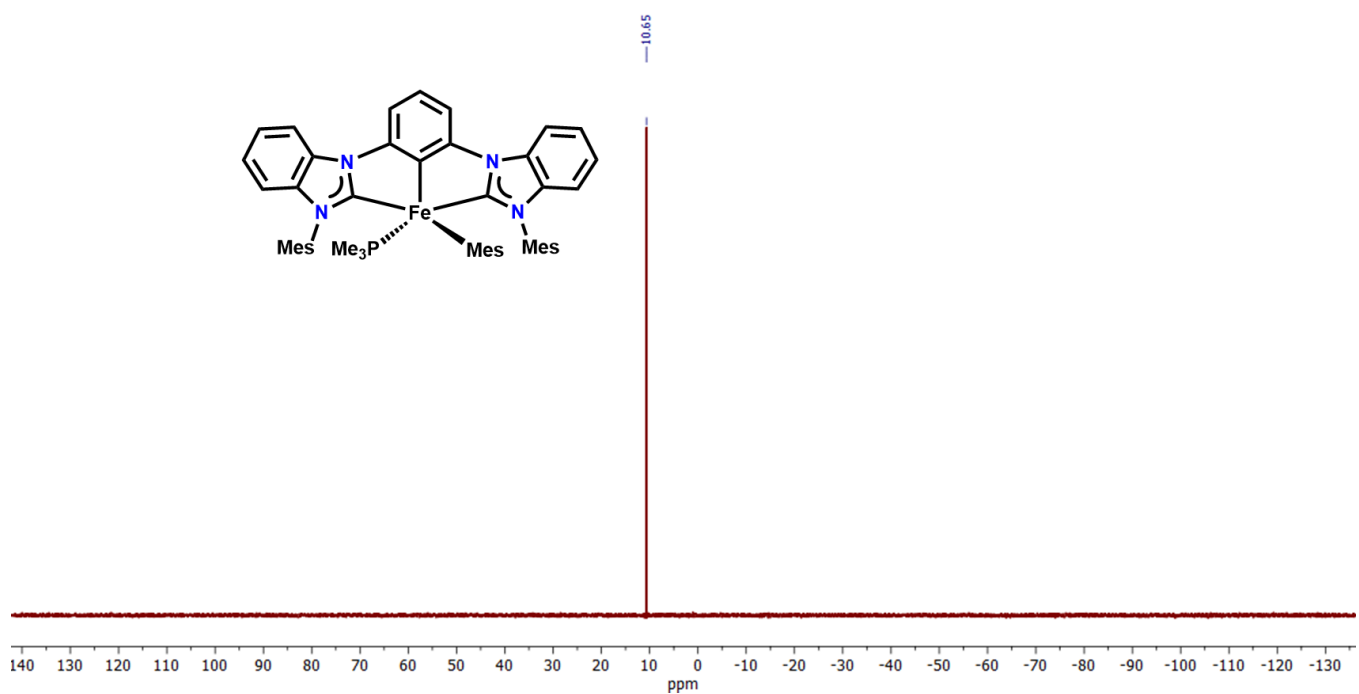
Figure S12. ^{31}P{^{1}H} NMR spectrum of **1-PMe₃** in C₆D₆.

NMR spectrum of [(^{Mes}CCC)FeMes]$_2$(μ–N$_2$)
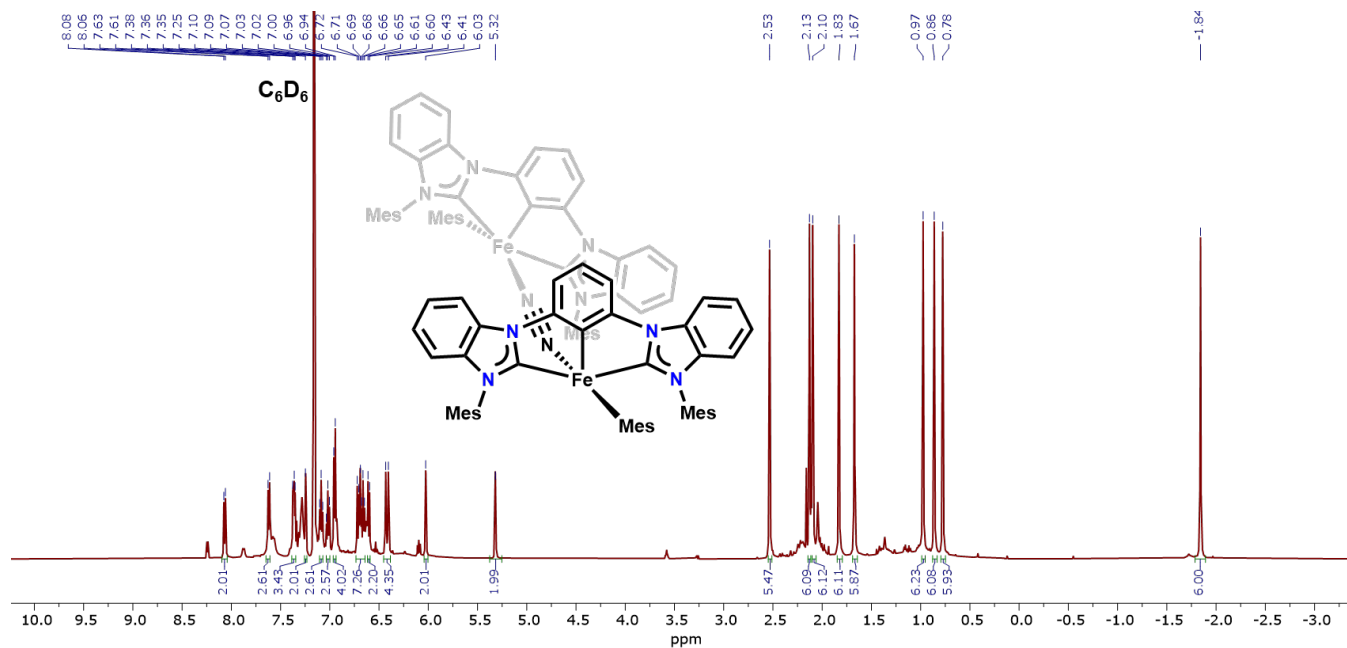
Figure S13. ^{1}H NMR spectrum of **1-N$_2$** in C$_6$D$_6$.

NMR spectra of (^{Mes}CCC)FeMes(CO)
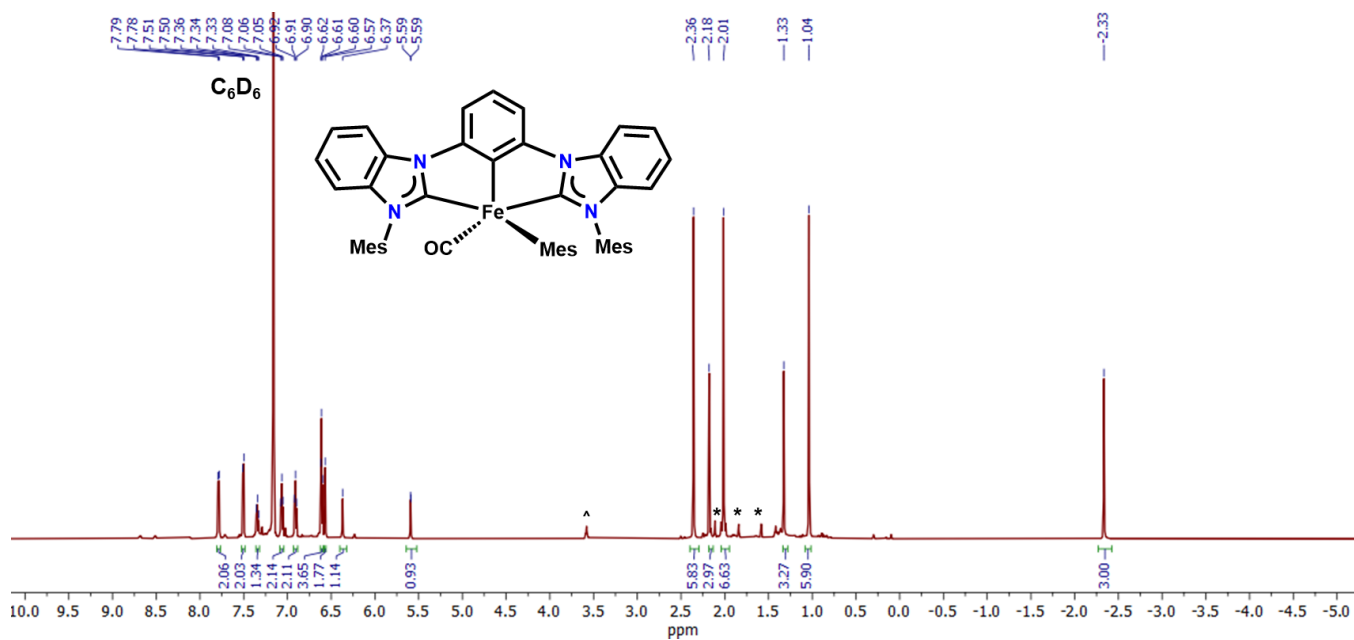
Figure S14. ^{1}H NMR spectrum of **1-CO** in C$_6$D$_6$ (^ denotes THF, * denotes **2**).

11
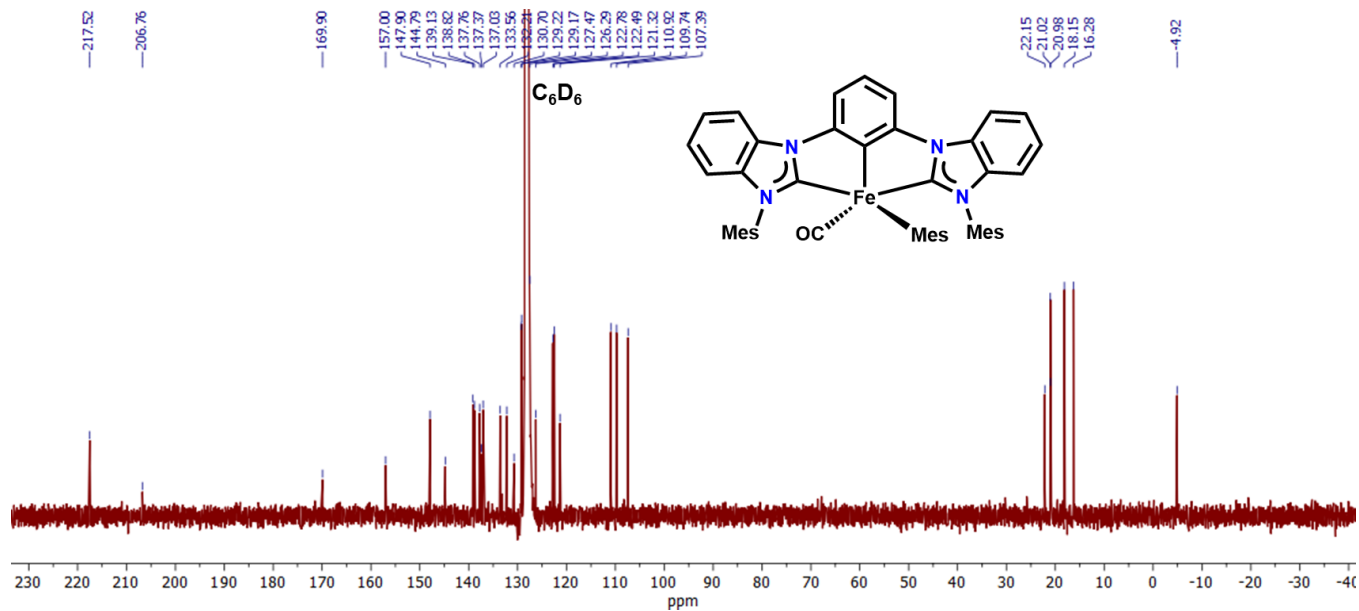
Figure S15. ^{13}C{^{1}H} NMR spectrum of **1-CO** in C$_6$D$_6$.

NMR spectra of (^{Mes}CCC)Fe(COMes)(CO)$_2$
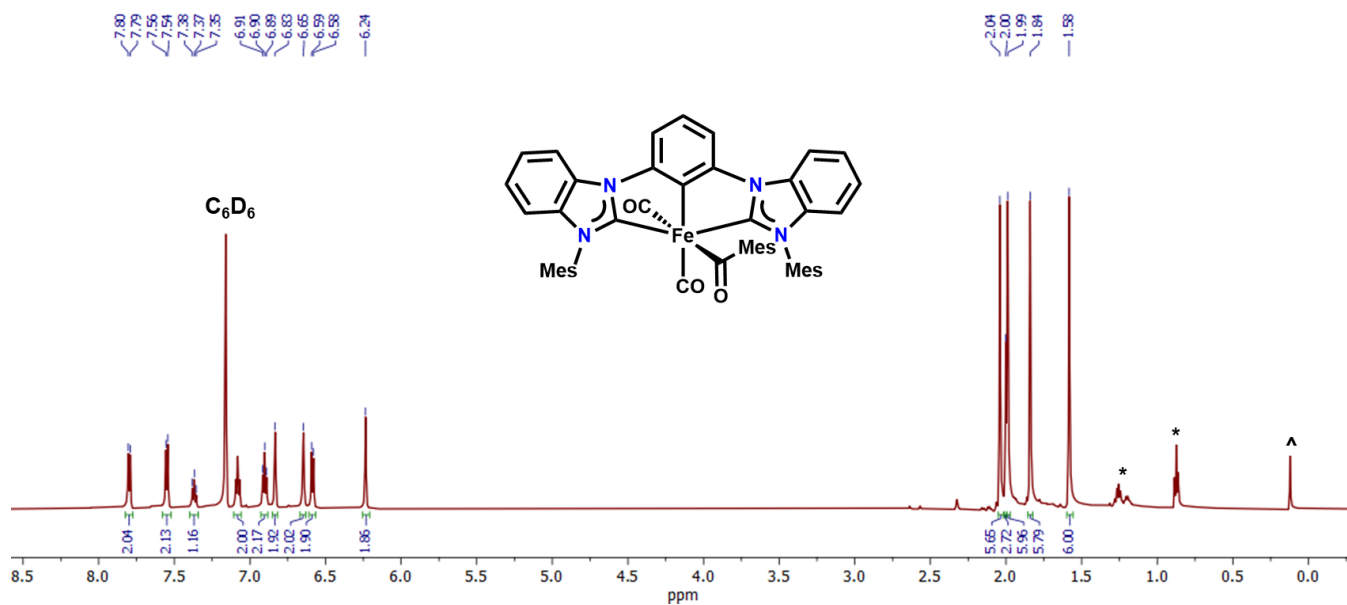
Figure S16. ^{1}H NMR spectrum of **2** in C$_6$D$_6$ (^ denotes HMDSO, * denotes pentane.
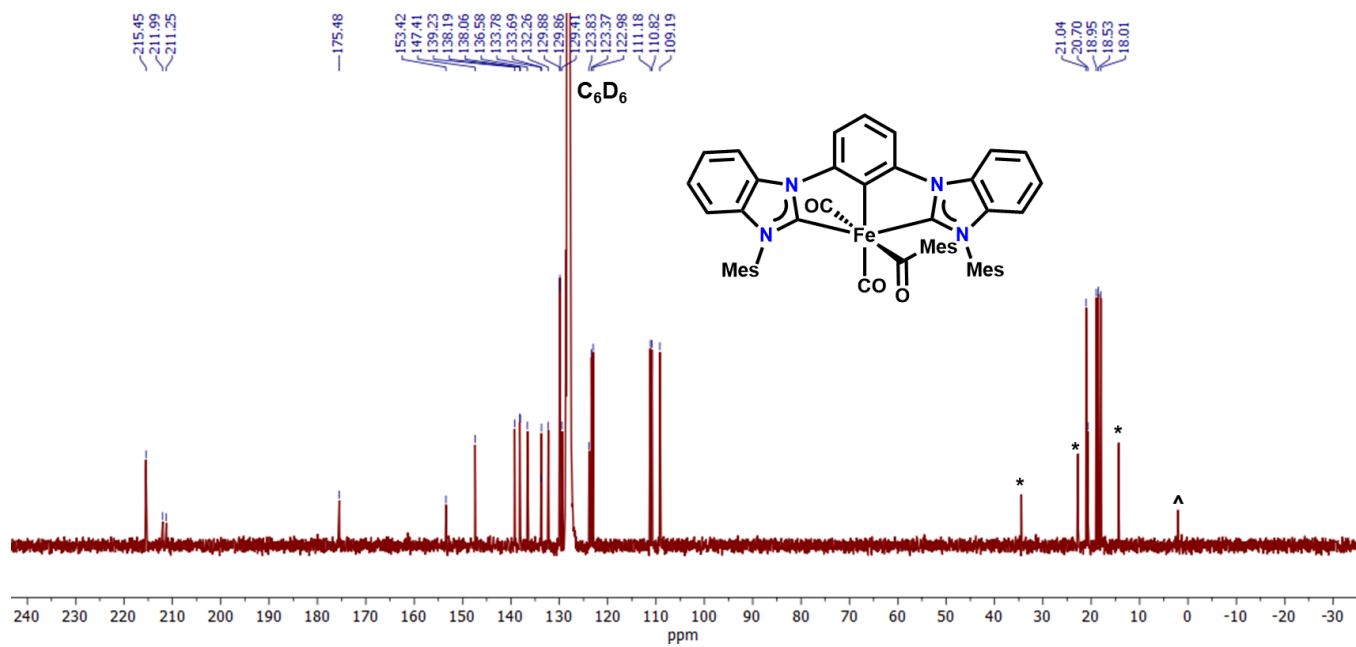
Figure S17. $^{13}C\{^1H\}$ NMR spectrum of **2** in C_6D_6 (^ denotes HMDSO, * denotes pentane).

ATR-IR spectra of 1-CO and 2
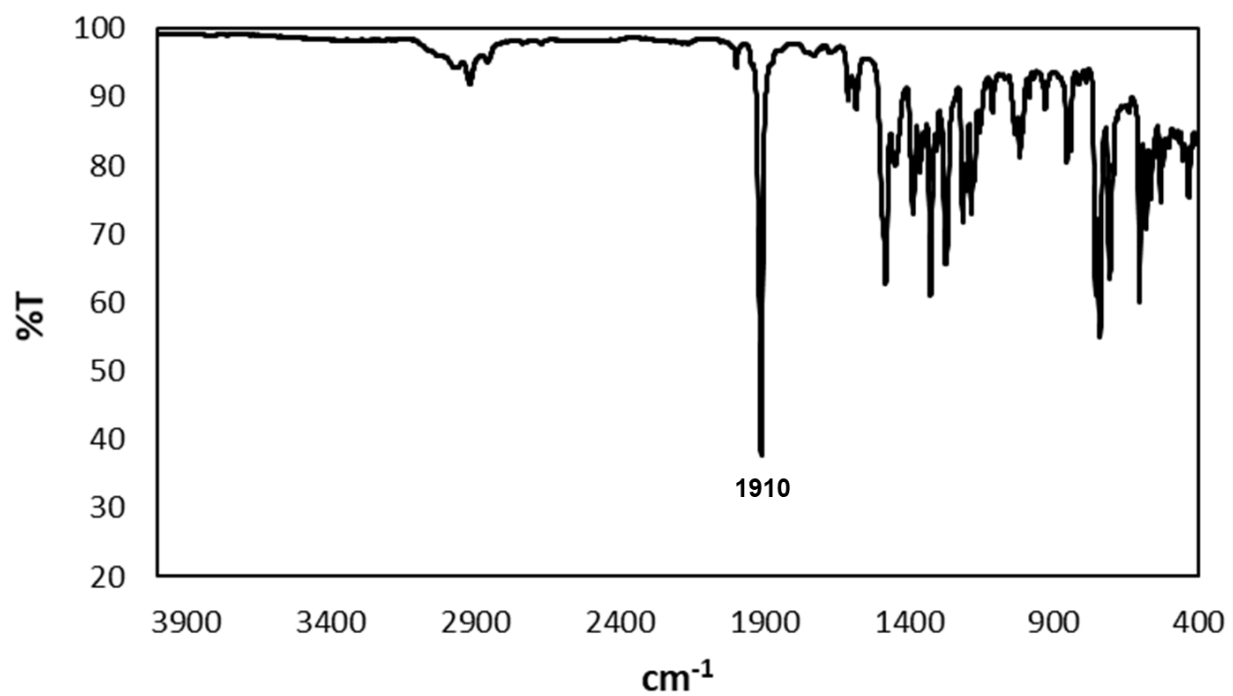
Figure S18. ATR-IR spectrum of **1-CO**.
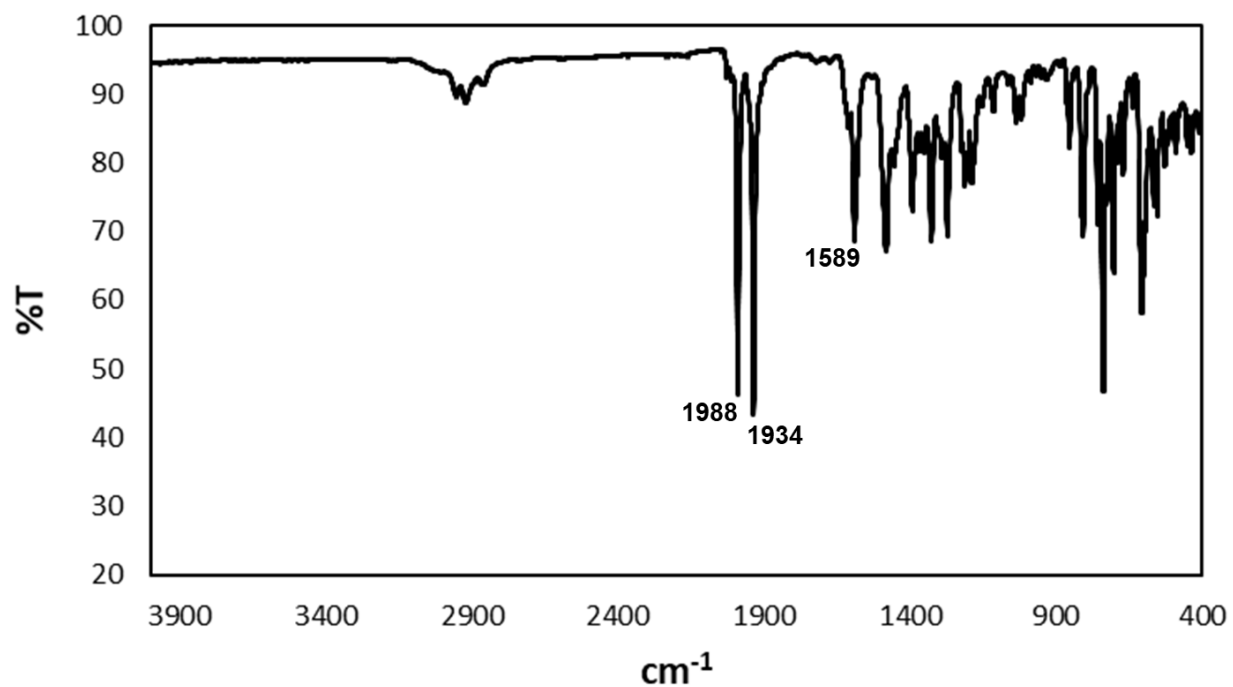
Figure S19. ATR-IR spectrum of **2**.

Solid-state structures of 1-L.

$\tau_5 = 0.01$

$(^{Mes}CCC)FeMes(Py)$ (**1-Py**)

$\tau_5 = 0.05$

$(^{Mes}CCC)FeMes(^{3,5}Lu)$ (**1-Lu**)

$\tau_5 = 0.18$

$(^{Mes}CCC)FeMes(PPh_3)$ (**1-PPh$_3$**)

$\tau_5 = 0.09$

$(^{Mes}CCC)FeMes(PMe_3)$ (**1-PMe$_3$**)

$\tau_5 = 0.02$

$(^{Mes}CCC)FeMes(MeCN)$ (**1-MeCN**)

$\tau_5 = 0.07$

$[(^{Mes}CCC)FeMes]_2(\mu\text{-}N_2)$ (**1-N$_2$**)
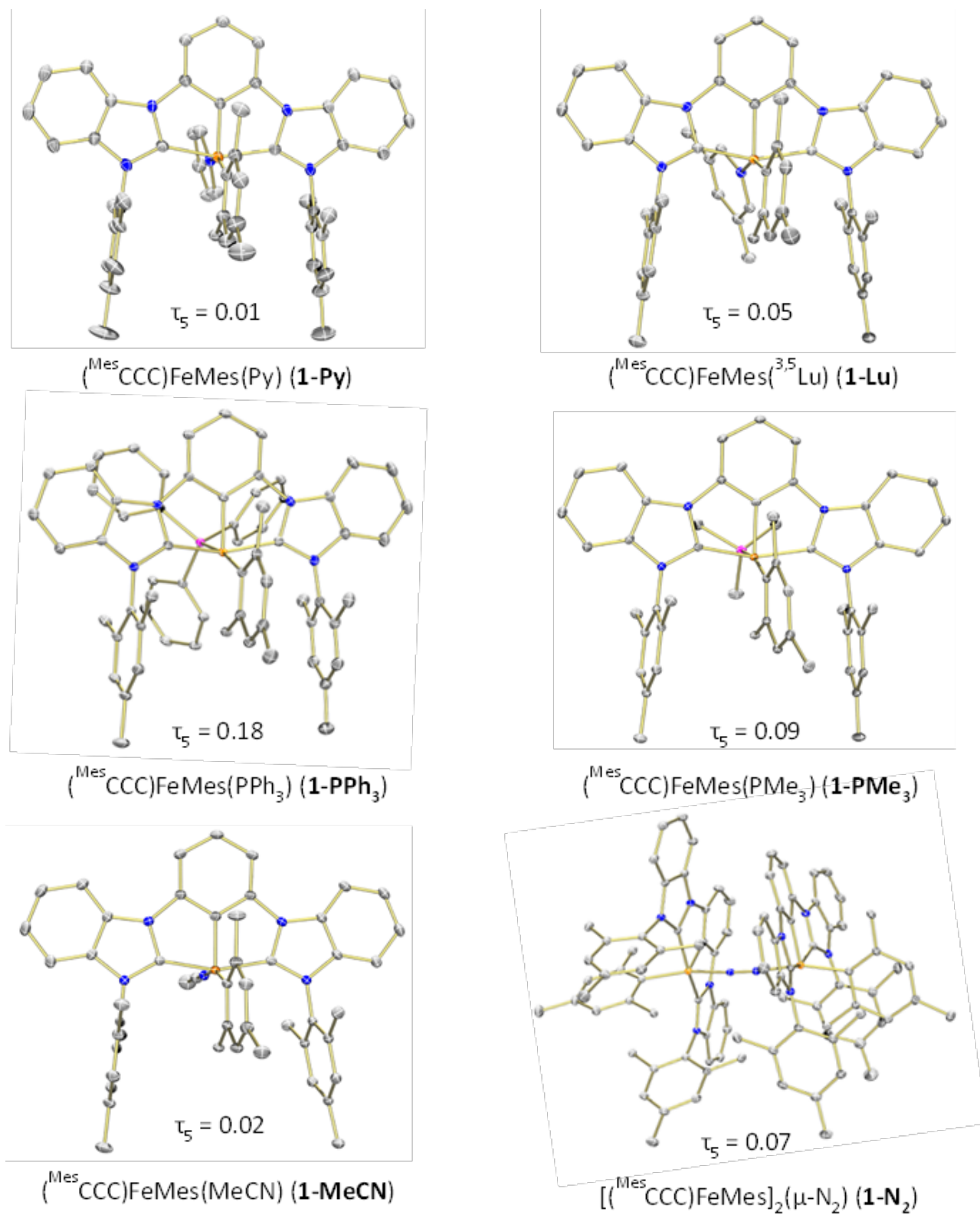
Figure S20. Molecular structures of **1-L** with 50% probability ellipsoids. Hydrogen atoms and solvent molecules have been omitted for clarity.

Crystallographic Parameters

Table S1. Crystallographic parameters for **1-Py**, **1-PPh₃**, and **1-Lu**.

	(^{Mes}CCC)FeMes(Py) **1-Py** ed27r	(^{Mes}CCC)FeMes(PPh₃) **1-PPh₃** ed02m	(^{Mes}CCC)FeMes(3,5-Lu) **1-Lu** ed02os
Empirical Formula	C52 H49 Fe N5	C72 H67 Fe N5 P	C54 H53 Fe N5
Formula Weight	799.81	1075.11	827.86
Temperature	100 K	130 K	100 K
Wavelength	0.71073 Å	0.71073 Å	0.71073 Å
Crystal system	Tetragonal	Triclinic	Monoclinic
Space group	$I4_1/a$	P-1	$P2_1/n$
Unit Cell Dimensions	$a = 22.9527(6)$ Å $b = 22.9527(6)$ Å $c = 43.0513(17)$ Å $\alpha = 90°$ $\beta = 90°$ $\gamma = 90°$	$a = 12.8919(5)$ Å $b = 13.2891(5)$ Å $c = 21.1112(7)$ Å $\alpha = 74.3660(10)°$ $\beta = 76.4280(10)°$ $\gamma = 89.3590(10)°$	$a = 12.2636(6)$ Å $b = 21.0134(10)$ Å $c = 17.2202(9)$ Å $\alpha = 90°$ $\beta = 92.9872(17)°$ $\gamma = 90°$
Volume	22680.6(15) Å^3	3380.5(2) Å^3	4431.6(4) Å^3
Z	24	2	4
Reflections collected	45634	135673	105251
Independent reflections	10393	16799	9092
Goodness-of-fit on F^2	1.032	1.035	1.026
Final R indexes [I>=2σ (I)]	$R_1 = 0.0541$ $wR_2 = 0.1221$	$R_1 = 0.0362$ $wR_2 = 0.0959$	$R_1 = 0.0390$ $wR_2 = 0.0860$

Table S2. Crystallographic parameters for **1-PMe₃**, **1-NCMe**, and **1-N₂**.

	(MesCCC)FeMes(PMe₃) **1-PMe₃** ed88s	(MesCCC)FeMes(NCMe) **1-NCMe** ed22n	[(MesCCC)FeMes]₂(μ-N₂) **1-N₂** ed41q
Empirical Formula	C58 H71 Fe N4 O Si2	C49 H44 D3 Fe N5	C100 H104 Fe2 N10
Formula Weight	959.16	764.78	1669.83
Temperature	100 K	130 K	100 K
Wavelength	0.71073 Å	0.71073 Å	0.71073 Å
Crystal system	Monoclinic	Monoclinic	Monoclinic
Space group	P2₁/n	P2₁/n	P2₁/n
Unit Cell Dimensions	$a = 12.0209(2)$ Å $b = 24.1592(3)$ Å $c = 17.9381(2)$ Å $\alpha = 90°$ $\beta = 92.99°$ $\gamma = 90°$	$a = 11.5262(2)$ Å $b = 18.7664(4)$ Å $c = 18.3183(4)$ Å $\alpha = 90°$ $\beta = 93.6900(10)°$ $\gamma = 90°$	$a = 15.2588(3)$ Å $b = 25.6179(5)$ Å $c = 23.7754(5)$ Å $\alpha = 90°$ $\beta = 92.0060(10)°$ $\gamma = 90°$
Volume	$5202.41(12)$ Å^3	$3954.13(14)$ Å^3	$9288.1(3)$ Å^3
Z	4	4	4
Reflections collected	82043	75733	216744
Independent reflections	12903	9825	17029
Goodness-of-fit on F^2	1.036	1.041	1.021
Final R indexes [I>=2σ (I)]	$R_1 = 0.0347$ $wR_2 = 0.0876$	$R_1 = 0.0373$ $wR_2 = 0.0940$	$R_1 = 0.0375$ $wR_2 = 0.0881$

Table S3. Selected bond distances and angles for **1-Py**, **1-PPh₃**, and **1-Lu**.

	(^{Mes}CCC)FeMes(Py) **1-Py**	(^{Mes}CCC)FeMes(PPh₃) **1-PPh₃**	(^{Mes}CCC)FeMes(3,5-Lu) **1-Lu**
Bond distances (Å)			
Fe–C$_{NHC}$	1.936(3)	1.9378(13)	1.9229(19)
Fe–C$_{NHC}$	1.947(3)	1.9491(12)	1.9530(18)
Fe–C$_{Ar}$	1.844(3)	1.8591(13)	1.8529(18)
Fe–C$_{Mes}$	1.965(3)	1.9914(13)	1.9744(18)
Fe···C$_{Agostic}$	2.702(3)	2.6823(14)	2.7238(19)
Fe–N	2.048(2)	N/A	2.0379(15)
Fe–P	N/A	2.3062(4)	N/A
Bond angles (°)			
C$_{NHC}$–Fe–C$_{NHC}$	159.38(10)	158.84(5)	159.51(7)
C$_{Ar}$–Fe–C$_{Mes}$	102.43(11)	101.48(5)	103.76(8)
C$_{Mes}$–Fe–N	159.90(10)	N/A	156.73(7)
C$_{Mes}$–Fe–P	N/A	169.66(4)	N/A

Table S4. Selected bond distances and angles for **1-PMe₃**, **1-NCMe**, and **1-N₂**.

	(^{Mes}CCC)FeMes(PMe₃) **1-PMe₃**	(^{Mes}CCC)FeMes(NCMe) **1-NCMe**	[(^{Mes}CCC)FeMes]₂(μ-N₂) **1-N₂**
Bond distances (Å)			
Fe–C$_{NHC1}$	1.9286(14)	1.9361(15)	1.9530(18), 1.9433(18)
Fe–C$_{NHC2}$	1.9441(14)	1.9229(15)	1.9400(18), 1.9443(18)
Fe–C$_{Ar}$	1.8589(13)	1.8581(15)	1.8707(18), 1.8720(18)
Fe–C$_{Mes}$	1.9806(14)	1.9634(16)	1.9673(19), 1.9622(18)
Fe···C$_{Agostic}$	2.6456(13)	2.7104(16)	2.710(2), 2.706(2)
Fe–N	N/A	1.9520(14)	1.8666(16), 1.8583(16)
Fe–P	2.2226(4)	N/A	N/A
N–N	N/A	N/A	1.135(2)
Bond angles (°)			
C$_{NHC}$–Fe–C$_{NHC}$	160.14(6)	160.22(6)	158.41(8), 158.27(7)
C$_{Ar}$–Fe–C$_{Mes}$	104.14(6)	103.40(7)	106.69(8), 105.56(8)
C$_{Mes}$–Fe–N	N/A	161.65(6)	162.50(7), 164.44(7)
C$_{Mes}$–Fe–P	165.38(4)	N/A	N/A

Computational Section

Density functional theory (DFT) calculations reported in this work were carried out using the dispersion corrected hybrid functional ωB97X-D[9] and the Gaussian09 software.[10] C, P and H atoms were described using the double-ζ basis set 6-31G(d,p), whereas the same basis set plus diffuse functions was employed to describe the more electronegative N and O atoms. Fe atoms were described using the effective core potential lanl2dz[11] including a f-polarization function (exponent = 2.462).[12] Geometry optimizations were performed in implicit benzene using the SMD solvation model[13] (ε = 2.2706) without imposing any constraint and using the X-ray structures when available. The nature of the stationary points was further verified to be energy minima through vibrational frequency analysis.

^{1}H NMR calculations in benzene were performed using the Gauge-Independent Atomic Orbital (GIAO) method.[14] The computed chemical shifts (in ppm) were referenced to tetramethylsilane, previously optimized in the same conditions. For the latter, the averaged value of the shifts, from the computationally inequivalent 12H atoms, was used as 0 for the computed NMR data collected in Table 1. Similarly, the averaged shift from the 3H atoms of the methyl group involved in the agostic interaction was used.[15]

Selected donor-acceptor interactions involved in the agostic bonds were assessed by means of Natural Bond Orbital (NBO) and Second Order Perturbation Theory (SOPT) analyses, using the NBO 7.0 program.[16]

The topology of the electron density was analysed by means of Quantum Theory of Atoms in Molecules (QTAIM),[17] as implemented in the Multiwfn package (version 3.7)[18] and using the inherited wavefunction from the geometry optimizations using Gaussian09.

Finally, the analysis of the non-covalent interactions (NCIs) was assessed using the Critic2 software,[19] and the above computed wavefunction, as we have reported recently.[20]

All the DFT data underlying this work, including the cartesian coordinates and NMR data of all the modelled structures, is openly accessible via the following ioChem-BD[21] online dataset:

https://iochem-bd.bsc.es/browse/review-collection/100/215759/2cb9163f47c1cdd9fa035a91

Table S5. Calculated GIAO isotropic magnetic shielding tensors (δ_{calc}) in benzene for the H atoms of the methyl groups involved in the agostic interactions. Averaged values ($\delta_{averaged}$) and ^{1}H NMR shifts (δ_{ref}) are referenced to TMS (calculated to be 31.74 ppm using the same methodology). All values are given in ppm.

Ligand	δ_{calc}			$\delta_{averaged}$	δ_{ref}
Lu	33.15	31.57	31.34	32.02	-0.28
Py	33.41	31.36	31.52	32.10	-0.36
NCMe	36.01	32.16	32.15	33.44	-1.70
PPh$_3$	36.12	31.76	32.03	33.30	-1.56
μ-N$_2{}^A$	36.55	32.43	32.59	33.86	-2.12
μ-N$_2{}^B$	36.54	32.56	32.42	33.84	-2.10
PMe$_3$	38.09	32.37	32.39	34.28	-2.54
CO	37.72	32.86	32.84	34.47	-2.73

*Note that for the dimeric complex **1-N$_2$**, two agostic interactions are observed, labelled with A and B in the Table.

Table S6. Selected NBO donor-acceptor interactions collected in Table 1, wherein the bonding C–H$_{agostic}$ orbital acts as a donor. The optimized structure of complexes with different ligands was analysed. *BD* and *BD** denote bonding and antibonding orbitals, respectively. ΔE_{SOPT} energies are given in kcal/mol.

Ligand	Donor	Contribution	Acceptor	Contribution	ΔE_{SOPT}
Lu	BD (1) C102–H104	60% C s (23%) p (77%) 40% H s (100%)	BD*(1) Fe1–C35	66% Fe s (6%) d (94%) 34% C s (29%) p (71%)	-10.7
Py	BD (1) C94–H96	60% C s (23%) p (77%) 40% H s (100%)	BD*(1) Fe1–C27	66% Fe s (6%) d (94%) 34% C s (29%) p (71%)	-11.6
NCMe	BD (1) C94–H95	60% C s (23%) p (77%) 40% H s (100%)	BD*(1) Fe1–C18	68% Fe s (26%) d (74%) 32% C s (29%) p (71%)	-18.8
PPh$_3$	BD (1) C69–H70	60% C s (23%) p (77%) 40% H s (100%)	BD*(1) Fe1–C7	68% Fe s (24%) d (76%) 32% C s (29%) p (71%)	-19.3
μ-N$_2{}^A$	BD (1) C187–H190	60% C s (23%) p (77%) 40% H s (100%)	BD*(1) Fe1–C35	67% Fe s (25%) d (75%) 33% C s (28%) p (72%)	-21.7
μ-N$_2{}^B$	BD (1) C191–H192	60% C s (23%) p (77%) 40% H s (100%)	BD*(1) Fe2–C36	67% Fe s (25%) d (75%) 33% C s (28%) p (72%)	-21.6
PMe$_3$	BD (1) C69–H70	60% C s (23%) p (77%) 40% H s (100%)	BD*(1) Fe1–C7	68% Fe s (24%) d (76%) 32% C s (29%) p (71%)	-22.6
CO	BD (1) C93–H94	60% C s (23%) p (77%) 40% H s (100%)	BD*(1) Fe1–C17	65% Fe s (23%) d (77%) 35% C s (28%) p (72%)	-20.3

*Note that for the dimeric complex **1-N$_2$**, two agostic interactions are observed, labelled with A and B in the Table.

Table S7. Main NBO donor-acceptor backdonation interaction (BD* C–H$_{agostic}$ as acceptor) identified for the complexes with different ligands. *BD* and *BD** denote bonding and antibonding orbitals, respectively. ΔE_{SOPT} energies are given in kcal/mol.

Ligand	Donor	Contribution	Acceptor	Contribution	ΔE_{SOPT}
Lu	BD (1) C95–C96$_{Mes}$	49% C95 p (100%) 51% C96 p (100%)	BD* (1) C102–H104	40% C s (23%) p (77%) 60% H s (100%)	-1.1
Py	BD (1) C87–C88$_{Mes}$	49% C87 p (100%) 51% C88 p (100%)	BD* (1) C94–H96	40% C s (23%) p (77%) 60% H s (100%)	-1.1
NCMe	BD (1) Fe1–C78$_{Mes}$	29% Fe s (32%) d (68%) 71% C s (28%) p (72%)	BD* (1) C94–H95	40% C s (23%) p (77%) 60% H s (100%)	-2.7
PPh$_3$	BD (1) Fe1–C67$_{Mes}$	32% Fe s (34%) d (66%) 68% C s (27%) p (73%)	BD* (1) C69–H70	40% C s (23%) p (77%) 60% H s (100%)	-3.0
μ-N$_2$^{A}	BD (1) Fe2–C155$_{Mes}$	31% Fe s (32%) d (68%) 69% C s (27%) p (73%)	BD* (1) C187–H192	40% C s (23%) p (77%) 60% H s (100%)	-3.0
μ-N$_2$^{B}	BD (1) Fe2–C156$_{Mes}$	31% Fe s (32%) d (68%) 69% C s (27%) p (73%)	BD* (1) C191–H192	40% C s (23%) p (77%) 60% H s (100%)	-3.0
PMe$_3$	BD (1) Fe1–C67$_{Mes}$	33% Fe s (34%) d (66%) 67% C s (27%) p (73%)	BD* (1) C69–H70	40% C s (23%) p (77%) 60% H s (100%)	-3.7
CO	BD (1) Fe1–C97$_{CO}$	28% Fe s (43%) d (57%) 72% C s (67%) p (33%)	BD* (1) C93–H94	40% C s (23%) p (77%) 60% H s (100%)	-5.9

*Note that for the dimeric complex **1-N$_2$**, two agostic interactions are observed, labelled with A and B in the Table.

Table S8. Selected NBO donor-acceptor interactions shown in Figure S23. *BD, BD** and *LV* denote bonding, antibonding and lone vacancy orbitals, respectively. ΔE_{SOPT} energies are given in kcal/mol.

Ligand	Donor	Contribution	Acceptor	Contribution	ΔE_{SOPT}
PMe$_3$ (1)	BD (1) C69–H70	60% C s (23%) p (77%) 40% H s (100%)	BD*(1) Fe1–C7	68% Fe s (24%) d (76%) 32% C s (29%) p (71%)	-22.6
PMe$_3$ (2)	BD (1) Fe1–C67$_{Mes}$	33% Fe s (34%) d (66%) 67% C s (27%) p (73%)	BD* (1) C69–H70	40% C s (23%) p (77%) 60% H s (100%)	-3.7
CO (3)	BD (1) Fe1–C97$_{CO}$	28% Fe s (43%) d (57%) 72% C s (67%) p (33%)	BD* (1) C93–H94	40% C s (23%) p (77%) 60% H s (100%)	-5.9
Lu (4)	BD (1) C102–H104	60% C s (23%) p (77%) 40% H s (100%)	LV (1) Fe1	Fe s (84%) d (16%)	-6.6

*Note that a similar interaction that the one shown in the table for Lu can be found in the Py analogue but no in the other complexes studied.

Table S9. Detailed NBO analysis for the complex **1-CO**. This includes all the donor-acceptor interactions with a cut-off of ΔE_{SOPT} = 1 kcal/mol, wherein BD or BD* orbitals of the C–H$_{agostic}$ are involved. *LP*, *BD, BD**, *RY* denote lone pairs, bonding, antibonding and Rydberg orbitals, respectively. ΔE_{SOPT} energies are given in kcal/mol.

Donor	*Contribution*	*Acceptor*	*Contribution*	ΔE_{SOPT}
LP (2) Fe1	d (100%)	BD* (1) C93–H94	40% C s (23%) p (77%) 60% H s (100%)	-1.6
BD (1) Fe1–C17	35% Fe s (23%) d (77%) 65% C s (28%) p (72%)	BD* (1) C93–H94	40% C s (23%) p (77%) 60% H s (100%)	-1.0
BD (1) Fe1–C36	26% Fe s (33%) d (67%) 74% C s (44%) p (56%)	BD* (1) C93–H94	40% C s (23%) p (77%) 60% H s (100%)	-2.6
BD (1) Fe1–C97$_{CO}$	28% Fe s (43%) d (57%) 72% C s (67%) p (33%)	BD* (1) C93–H94	40% C s (23%) p (77%) 60% H s (100%)	-5.9
BD (1) C93–H94	60% C s (23%) p (77%) 40% H s (100%)	BD*(1) Fe1–C17	65% Fe s (23%) d (77%) 35% C s (28%) p (72%)	-20.3
BD (1) C93–H94	60% C s (23%) p (77%) 40% H s (100%)	BD*(1) Fe1–C36	74% Fe s (33%) d (67%) 26% C s (44%) p (56%)	-1.8
BD (1) C93–H94	60% C s (23%) p (77%) 40% H s (100%)	BD*(1) Fe1–C97	72% Fe s (43%) d (57%) 28% C s (67%) p (33%)	-1.2
BD (1) C93–H94	60% C s (23%) p (77%) 40% H s (100%)	RY (2) Fe1	p (95%) d (5%)	-2.8
BD (1) C93–H94	60% C s (23%) p (77%) 40% H s (100%)	RY (3) Fe1	s (80%) p (15%) d (5%)	-2.4
BD (1) C93–H94	60% C s (23%) p (77%) 40% H s (100%)	RY (1) O98	s (84%) p (6%) d (10%)	-1.1
BD (1) C93–H94	60% C s (23%) p (77%) 40% H s (100%)	BD*(1) C90–C92$_{Mes}$	50% C s (36%) p (64%) 50% C s (35%) p (65%)	-2.5

Table S10. Selected QTAIM data at the bond critical points (BCPs) and relevant atomic charges (in a.u.).

Ligand	*Fe···H BCP*		*C–H BCP*		*AIM charges*		
	$\rho(r)$	$\nabla^2\rho(r)^a$	$\rho(r)$	$\nabla^2\rho(r)^a$	q_H	q_{Fe}	q_C
Lu	0.021	+0.090	0.268	-0.872	-0.042	0.913	-0.020
Py	0.021	+0.097	0.267	-0.865	-0.052	0.925	-0.021
NCMe	0.021	+0.128	0.263	-0.839	-0.072	0.911	0.002
PPh$_3$	0.025	+0.125	0.264	-0.843	-0.062	0.816	-0.003
μ-N$_2$^{b}	0.025	+0.133	0.262	-0.830	-0.071	0.902	0.016
PMe$_3$	0.025	+0.140	0.261	-0.827	-0.064	0.795	0.004
CO	0.027	+0.146	0.260	-0.818	-0.079	0.863	0.019

[a]Note that in the case of the electron density topology, the sign of the Laplacian of the electron density at the (3, −1) BCP is determined by the nature of the interaction; covalent interactions are characterized by a negative value of the Laplacian, whereas, non-covalent interactions have associated a positive value. [b]Averaged values between the two agostic bonds in the dimeric complex.
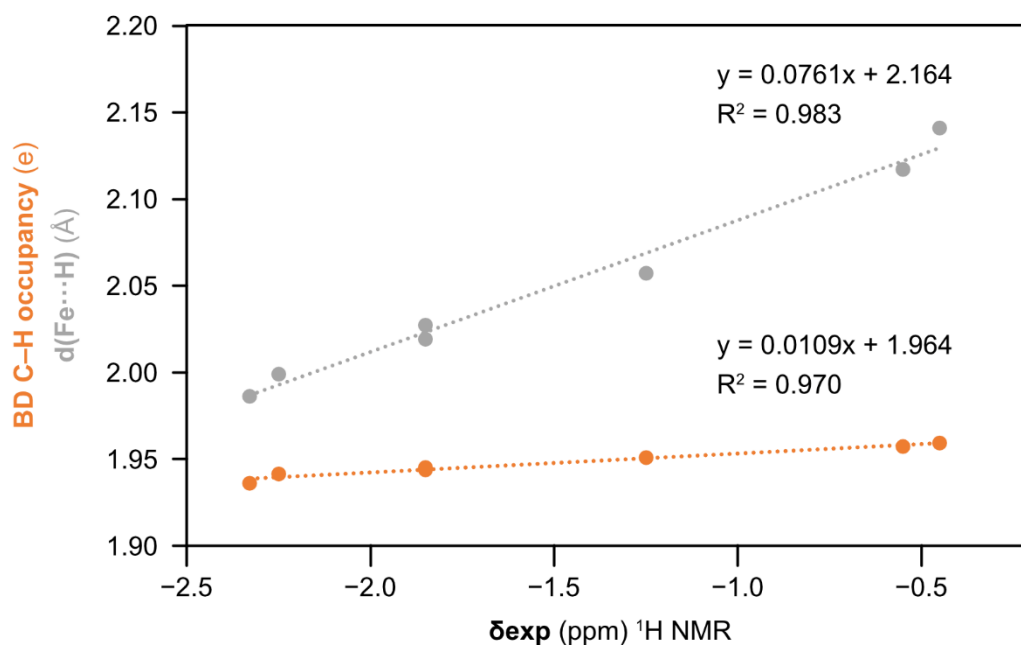
Figure S21. Linear correlations found between the experimental ^{1}H NMR shifts (x-axis) and: *i)* the computed Fe···H distances (grey trace); *ii)* the NBO occupancy of the BD C–H$_{agostic}$ orbital (orange trace). The equations and Pearson correlation coefficients of the linear fits are included in the plot.

Background of non-covalent interaction (NCI) analysis

This section is devoted to providing a brief overview of the fundamental theory behind the NCI analysis. For a more detailed description, we refer the reader to the original work by Contreras-García, *et al.*[22]

Electron density regions where the reduced density matrix tends to zero are characterized by a reduced density gradient, which also tends to zero, indicating an inflection point between two density maxima. The reduced density gradient (s, plotted in the y-axis of the NCI plots) is a function of the gradient of the electron density (ρ), according to the equation:

$$s(\mathbf{r}) = \frac{1}{2(3\pi^2)^{\frac{1}{3}}} \frac{|\nabla \rho(\mathbf{r})|}{\rho(\mathbf{r})^{\frac{4}{3}}}$$

The actual electron density at these points can be related to the interaction strength, *i.e.* the larger the electron density the more intense is the interaction. In addition, the attractive or repulsive nature of the interaction can be assessed by investigating the curvature of the electron density, $\nabla^2 \rho$.

Since the overall curvature is dominated by attractive electron-core interactions, the local curvatures in the diagonalized Hessian of the electronic density matrix (containing the second order partial derivatives) are considered. Specifically, the second eigenvalue of the Hessian matrix, λ_2, has been shown to be a good indicator of the interaction behavior, as it becomes negative when the interaction is attractive and positive when it is repulsive. Therefore, by analyzing the reduced density gradient at all points of the electron density, and plotting s as a function of sign(λ_2)ρ (x-axis in the NCI plots), we can identify the interactions as peaks in the electron density.
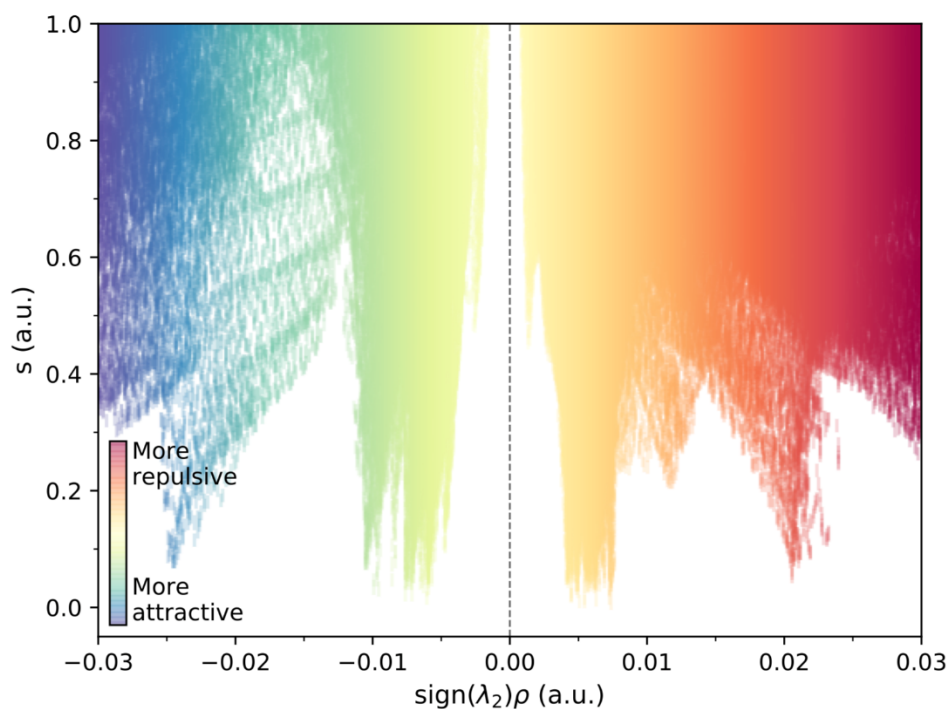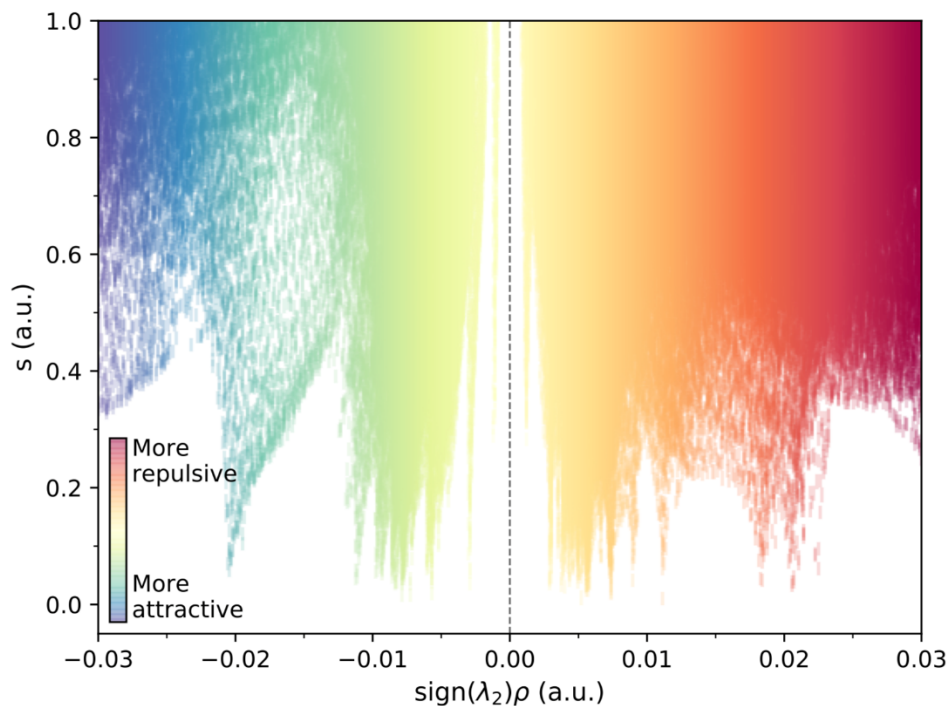
Figure S22. Calculated NCI plots for the complexes **1-Lu** (top) and **1-PMe₃** (bottom). These plots represent the reduced density gradient (*s*) as a function of the electron density (ρ) multiplied by the sign of the second eigenvalue of the Hessian matrix (sign(λ_2)ρ), which effectively displays the NCIs as distinct peaks. Colder/warmer colors depict attractive/repulsive interactions. The Fe⋯H agostic interactions correspond to the blue peak in both cases (x value of *ca.* −0.020 for **1-Lu** and *ca.* −0.025 for **1-PMe₃**).

BD CH → BD* FeC$_{trans}$
$E_{SOPT} = -22.6$ (PMe$_3$)

BD CH → LV Fe
$E_{SOPT} = -6.6$ (Lu)

BD FeC$_{Mes}$ → BD* CH
$E_{SOPT} = -3.7$ (PMe$_3$)

BD FeC$_{CO}$ → BD* CH
$E_{SOPT} = -5.9$ (CO)
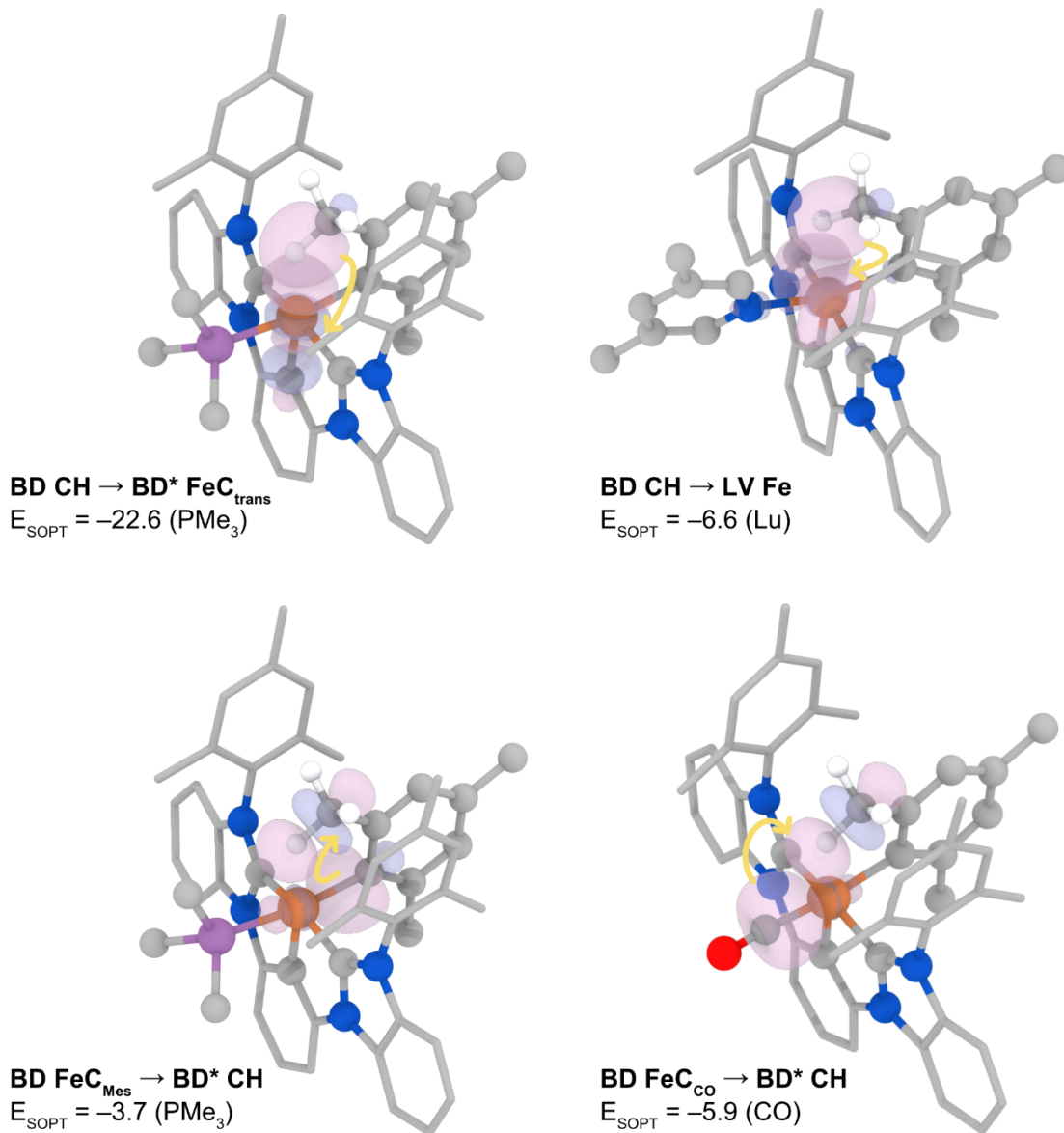
Figure S23. Representation of the isosurfaces (isovalue = 0.07 a.u) of selected donor−acceptor NBO interactions for complexes with different ligands (specified in parenthesis). All the relevant data is gathered in Table S8. The yellow arrows indicate the direction of electron donation (from the donor to the acceptor). Most H atoms have been omitted for clarity. ΔE_{SOPT} energies are given in kcal/mol.

References

1. A. B. Pangborn, M. A. Giardello, R. H. Grubbs, R. K. Rosen and F. J. Timmers, *Organometallics*, 1996, **15**, 1518–1520.
2. A. D. Ibrahim, K. Tokmic, M. R. Brennan, D. Kim, E. M. Matson, M. J. Nilges, J. A. Bertke and A. R. Fout, *Dalt. Trans.*, 2016, **45**, 9805–9811.
3. G. E. . Martinez, J. A. Killion, B. J. Jackson and A. R. Fout, *Inorg. Synth.,* 2018, **37**, 50–55.
4. APEX2; Bruker AXS, Inc.: Madison, WI, 2004.
5. L. Krause, R. Herbst-Irmer, G. M. Sheldrick and D. Stalke, *J. Appl. Crystallogr.* 2015, **48**, 3−10.
6. G. M. Sheldrick, *Acta Cryst.,* 2015, **A71**, 3−8.
7. G. M. Sheldrick, *Acta Cryst.,* 2015, **C71**, 3−8.
8. O. V. Dolomanov, L. J. Bourhis, R. J. Gildea, J. A. K. Howard and H. Puschmann, *J. Appl. Crystallogr.* 2009, **42**, 339−341.
9. J.-D. Chai and M. Head-Gordon, *Phys. Chem. Chem. Phys.*, 2008, **10**, 6615–6620.
10. Gaussian 09, Revision **E.01**, M. J. Frisch, G. W. Trucks, H. B. Schlegel, G. E. Scuseria, M. A. Robb, J. R. Cheeseman, G. Scalmani, V. Barone, G. A. Petersson, H. Nakatsuji, X. Li, M. Caricato, A. V. Marenich, J. Bloino, B. G. Janesko, R. Gomperts, B. Mennucci, H. P. Hratchian, J. V. Ortiz, A. F. Izmaylov, J. L. Sonnenberg, D. Williams-Young, F. Ding, F. Lipparini, F. Egidi, J. Goings, B. Peng, A. Petrone, T. Henderson, D. Ranasinghe, V. G. Zakrzewski, J. Gao, N. Rega, G. Zheng, W. Liang, M. Hada, M. Ehara, K. Toyota, R. Fukuda, J. Hasegawa, M. Ishida, T. Nakajima, Y. Honda, O. Kitao, H. Nakai, T. Vreven, K. Throssell, J. A., Jr. Montgomery, J. E. Peralta, F. Ogliaro, M. J. Bearpark, J. J. Heyd, E. N. Brothers, K. N. Kudin, V. N. Staroverov, T. A. Keith, R. Kobayashi, J. Normand, K. Raghavachari, A. P. Rendell, J. C. Burant, S. S. Iyengar, J. Tomasi, M. Cossi, J. M. Millam, M. Klene, C. Adamo, R. Cammi, J. W. Ochterski, R. L. Martin, K. Morokuma, O. Farkas, J. B. Foresman, D. J. Fox, Gaussian, Inc., Wallingford CT, 2009.
11. (a) P. J. Hay and W. R. Wadt, *J. Chem. Phys.*, 1985, **82**, 270–283. (b) P. J. Hay and W. R. Wadt, *J. Chem. Phys.*, 1985, **82**, 299–310.
12. A. W. Ehlers, M. Böhme, S. Dapprich, A. Gobbi, A Höllwarth, V. Jonas, K. F. Köhler, R. Stegmann, A. Veldkamp and G. Frenking, *Chem. Phys. Lett.*, 1993, **208**, 111–114.
13. A. V. Marenich, C. J. Cramer and D. G. Truhlar, *J. Phys. Chem. B*, 2009, **113**, 6378–6396.
14. J. R. Cheeseman, G. W. Trucks, T. A. Keith and M. J. Frish, *J. Phys. Chem.*, 1996, **104**, 5497‑5509.
15. Note that only one signal for this methyl group was observed in the ^{1}H NMR spectra, due to fast rotation for the NMR timescale at room temperature
16. NBO 7.0. E. D. Glendening, J. K. Badenhoop, A. E. Reed, J. E. Carpenter, J. A. Bohmann, C. M. Morales, P. Karafiloglou, C. R. Landis and F. Weinhold, Theoretical Chemistry Institute, University of Wisconsin, Madison, WI (2018).
17. R. F. W. Bader, Atoms in Molecules: A Quantum Theory; Oxford University Press, 1990.
18. T. Lu and F. Chen, *J. Comput. Chem.*, 2012, **33**, 580–592.
19. A. Otero-de-la-Roza, E. R. Johnson and V. Luaña, *Comput. Phys. Commun.*, 2014, **185**, 1007–1018.
20. Y. J. Park, M. N. Peñas-Defrutos, M. J. Drummond, Z. Gordon, O. R. Kelly, I. J. Garvey, K. L. Gullett, M. García-Melchor and A. R. Fout, *Inorg. Chem.*, 2022, **61**, 8182–8192.
21. M. Álvarez-Moreno, C. de Graaf, N. López, F. Maseras, J. M. Poblet and C. Bo, *J. Chem. Inf. Model.*, 2015, **55**, 95−103.
22. J. Contreras-García, E. R. Johnson, S. Keinan, R. Chaudret, J.-P. Piquemal, D. N. Beratan and W. Yang, *J. Chem. Theory Comput.*, 2011, **7**, 625−632.